REVIEW ARTICLE   OPEN

Understanding and designing magnetoelectric heterostructures guided by computation: progresses, remaining questions, and perspectives

Jia-Mian Hu[1], Chun-Gang Duan[2], Ce-Wen Nan[3] and Long-Qing Chen[1]

Magnetoelectric composites and heterostructures integrate magnetic and dielectric materials to produce new functionalities, e.g., magnetoelectric responses that are absent in each of the constituent materials but emerge through the coupling between magnetic order in the magnetic material and electric order in the dielectric material. The magnetoelectric coupling in these composites and heterostructures is typically achieved through the exchange of magnetic, electric, or/and elastic energy across the interfaces between the different constituent materials, and the coupling effect is measured by the degree of conversion between magnetic and electric energy in the absence of an electric current. The strength of magnetoelectric coupling can be tailored by choosing suited materials for each constituent and by geometrical and microstructural designs. In this article, we discuss recent progresses on the understanding of magnetoelectric coupling mechanisms and the design of magnetoelectric heterostructures guided by theory and computation. We outline a number of unsolved issues concerning magnetoelectric heterostructures. We compile a relatively comprehensive experimental dataset on the magnetoelecric coupling coefficients in both bulk and thin-film magnetoelectric composites and offer a perspective on the data-driven computational design of magnetoelectric composites at the mesoscale microstructure level.

INTRODUCTION

Computational modeling has become an imperative component of modern materials research. It provides fundamental insights into experimental observations, and more excitingly, guidance to experiments to achieve or optimize a desirable property or functionality. A new paradigm has recently emerged[1–7] that uses informatics tools to understand and harness existing data of materials structure and properties, aiming at generating statistically correct computer models for predicting properties of a material structure and inversely, designing a material structure that optimizes a property or set of properties. Such data-driven computational materials design (see Fig. 1) is expected to accelerate the materials discovery and application, as outlined in the US Materials Genome Initiative.[8]

In this article, we review recent progresses in computational modeling of magnetoelectric heterostructures. After an introduction to magnetoelectric heterostructures and different mechanisms of magnetoelectric coupling, we show how computational methods such as density functional theory (DFT) calculations, phase-field method, and finite-element calculations have been utilized for understanding the magnetoelectric coupling mechanisms at multiple scales (corresponding to the *top layer* in Fig. 1), predicting new types of magnetoelectric couplings, and designing magnetoelectric heterostructures for optimum device performances (the *middle layer* in Fig. 1). Several remaining questions concerning magnetoelectric heterostructures are then discussed.

We compile a rather comprehensive dataset of magnetoelectric coupling coefficients of magnetoelectric composites and heteostructures, and briefly discuss the perspective for implementing a data-driven computational design of magnetoelectric composites (the *bottom layer* in Fig. 1) through machine learning. There exist a number of comprehensive reviews (see recent ones in refs 9–13) concerning magnetoelectric materials. Here we focus on the guidance provided by theory and computation on understanding and designing magnetoelectric materials.

Mechanisms of magnetoelectric coupling in magnetoelectric composites/heterostructures

Magnetoelectric heterostructures allow the constituting magnetic and dielectric materials to interact such that the electrical response of the dielectric material can be modulated by magnetically stimulating the magnetic material, and vice versa. Specifically, applying a magnetic field (H) can modulate electric polarization (P), $\Delta P = \alpha_H \Delta H$, or electric field ($E$), $\kappa_0 \chi_e \Delta E = \alpha_H \Delta H$, where κ_0 is vacuum permittivity and χ_e the electric susceptibility; conversely, applying an electric field can modulate magnetization (M), $\mu_0 \Delta M = \alpha_E \Delta E$, where μ_0 is the vacuum permeability; α_H and α_E are the direct and converse magnetoelectric coupling coefficients, respectively. Therefore, magnetoelectric heterostructures enable the conversion between magnetic energy and electric energy in the absence of an electric current, and thus a number of promising applications. For instance, one can detect a target

[1]Department of Materials Science and Engineering, Pennsylvania State University, University Park, PA 16802, USA; [2]Key Laboratory of Polar Materials and Devices, Ministry of Education, East China Normal University, Shanghai, China and [3]School of Materials Science and Engineering, and State Key Lab of New Ceramics and Fine Processing, Tsinghua University, Beijing 100084, China
Correspondence: Jia-Mian Hu (juh34@psu.edu) or Long-Qing Chen (lqc3@psu.edu)

npj

Understanding and designing magnetoelectric heterostructures
J-M Hu et al.

2
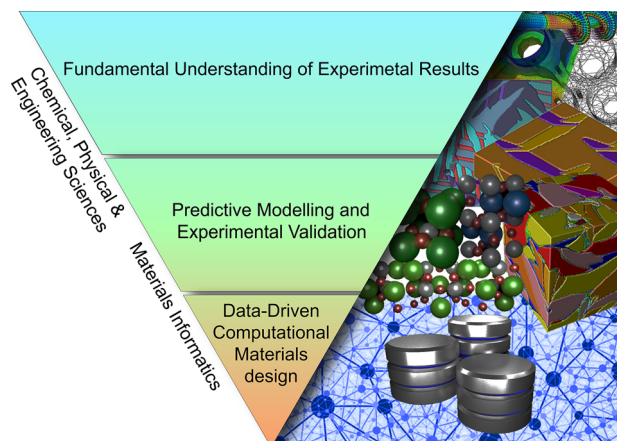
Fig. 1 Illustration of three primary roles of computational modeling in materials research and design

Fig. 2 **a** Classifying magnetoelectric (magnetic/dielectric) hetero-structures by the functionality of the dielectric materials, along with the representative dielectric materials. The solid ellipses suggest the corresponding mechanisms of converse magnetoelectric coupling. Schematics explaining the mechanisms of converse magnetoelectric coupling enabled through electric field modulation of **b** spin-polarized electron densities, **c** degree of interfacial oxidation, **d** strain, and **e** exchange coupling. In **b** the change of electron densities shifts the Fermi level E_F and hence the LDOS. In **c** the details of how the interfacial oxide (MO_x) layer affects the magnetic anisotropy of the overlaying metal M remain unclear (see the section of Remaining questions). In **e** only one single AF domain with perpendicular sublattice magnetizations (see *arrows* in the bottom layer) is shown for simplicity. The exchange coupling arises from the Heisenberg-type exchange interaction between the uncompensated surface magnetization (canted magnetization in $BiFeO_3$) and the local magnetization at the bottom of the magnet. Note that the converse magnetoelectric coupling illustrated in **c** involves the exchange of both matter and energy across the interface (that is, through an interfacial redox reaction), whereas the coupling illustrated in **a**, **b**, **d**, and **e** only involve the exchange of (magnetic, elastic, electric) energy. *FE-AF* Ferroelectric-antiferromagnetic, *ME-AF*: Magnetoelectric-antiferromagnetic, *BTO* $BaTiO_3$, *PZT* $Pb(Zr,Ti)O_3$, *PMN-PT* $[Pb(Mg_{1/3}Nb_{2/3})O_3]_{1-x}$-$[PbTiO_3]_x$, *PZN-PT* $Pb(Zn_{1/3}Nb_{2/3})O_3]_{1-x}$-$[PbTiO_3]_x$

magnetic field by analyzing its induced output electric voltage, working as a portable, low-cost magnetic field sensor that may replace the cumbersome, expensive superconducting quantum interface device for noninvasive medical imaging and diagnosis;[14, 15] one can also use an electric field rather than an electric current to drive the rotation of a magnetization vector, completing an electric-write process in magnetic memories with a negligible amount of heat dissipation. More detailed discussions on the applications of magnetoelectric materials have been summarized in a number of recent articles.[16–19]

In general, magnetoelectric coupling in composites and heterostructures relies on the interplay among the spin, orbit, charge, and lattice degrees of freedom across the interfaces (more precisely, the interphase boundaries). This is different from the case in single-phase multiferroics (materials with coexistence of two or more primary ferroic orders, see recent reviews[9, 20]), where the magnetoelectric coupling arises from the interplay among the above-mentioned four fundamental degrees of freedom within one crystal lattice. Direct magnetoelectric coupling (that is, magnetic field control of electric polarization) in magnetoelectric heterostructures has so far only been observed to occur through one single mechanism: magnetic-field-induced strain is transferred to a piezoelectric layer across the interface, and then such strain modulates the electric polarization through the piezoelectric coupling. Converse magnetoelectric coupling (that is, electric field control of magnetism) in magnetoelectric heterostructures, in contrast, can occur through multiple mechanisms. Notably, the number of different mechanisms that the converse magneto-electric coupling in a magnetoelectric heterostructure could possibly have is implied by the functionality of the constituent dielectric material (see Fig. 2a). For example, if the constituent dielectric layer is a pure dielectric (the *outermost circle* in Fig. 2), the converse magnetoelectric coupling will occur through at most two different mechanisms (indicated by the *solid ellipses* in Fig. 2a). If the constituent dielectric layer is a ferroelectric-antiferromagnet (FE-AF), the number of possible converse magnetoelectric coupling mechanisms will be four, and so forth. Below we will discuss the converse magnetoelectric coupling mechanisms in different magnetoelectric heterostructures whose constituent dielectric layers range from a pure dielectric to a complex FE-AF (from *outmost* to *innermost* circle in Fig. 2a). The advantages/disadvantages of implementing converse magnetoelectric coupling of different mechanisms will also be briefly discussed.

Electric field modulated spin-polarized charge densities. When the dielectric layer is a pure dielectric with poor ionic conductivity
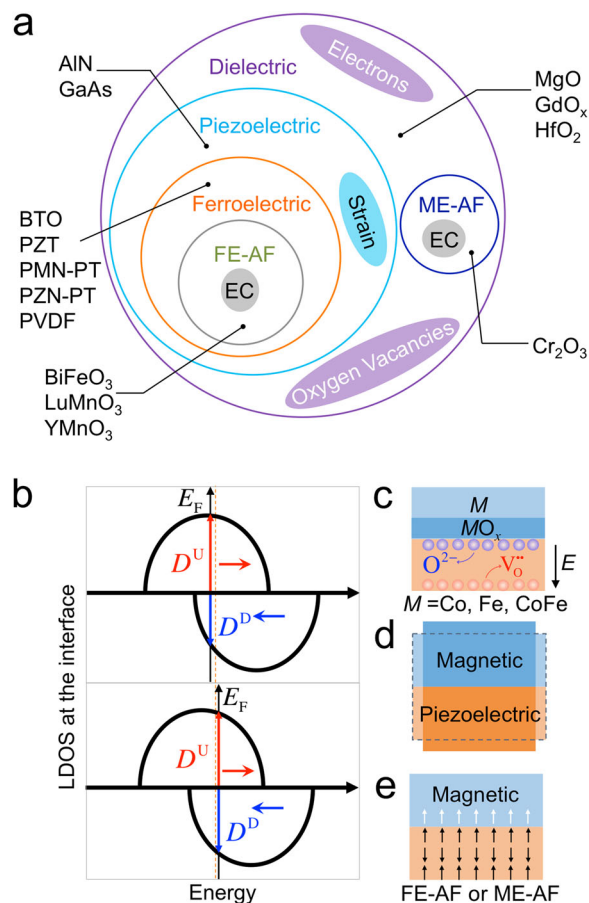
(e.g., MgO with low concentration of ionic defects, see Fig. 2a), modulation of the spin polarization and magnetic moment[21, 22] at the interface occurs through the modulation of the surface electron density of the dielectric as a voltage is applied. Let us first discuss how the interface spin polarization can be electrically modulated. An electrically enhanced (reduced) surface electron density of the dielectric would reduce (enhance) the electron density in the magnetic layer through the electrostatic interaction, which would shift the Fermi energy (E_F) in the interface region of

Understanding and designing magnetoelectric heterostructures
J-M Hu et al.

npj

3

the magnet to a lower (higher) level. Based on the thermodynamics of electronic defects proposed by Maier et al.,[23] we propose that such electrically shifted Fermi energy can be estimated by $\Delta E_F = E_F(E) - E_F(E=0) = k_B T \ln[(n_0 + \Delta n)/n_0]$, where the k_B is the Boltzmann constant, n_0 the electron density under zero electric field ($E = 0$); $\Delta n = -\kappa_0 \kappa_r \Delta E$ is the change of the spin-polarized screening electron density in the interface region of the magnet, where κ_r is the relatively permittivity. As schematically shown in Fig. 2b, shifting E_F can modulate the local density of states (LDOS) and thereby modulate the spin polarization $\eta = (D^U - D^D)/(D^U + D^D)$ with $0 < \eta \leq 1$, where D^D and D^U represent the LDOS of the spin-down and spin-up electrons, respectively. First-principles DFT calculations can be utilized to quantify such a LDOS change. Furthermore, the voltage-induced interface magnetic moment (Δm) is given by $\Delta m = (\Delta n \eta \mu_B)/e$,[24] where μ_B is the Bohr magneton and e the elementary charge. These analyses suggest that magnetoelectric heterostructures with a higher κ_r dielectric layer should exhibit a larger change in both the interface spin polarization and magnetic moment. Furthermore, if employing a ferroelectric that has an electric-field-switchable spontaneous polarization as the dielectric, a nonvolatile voltage-modulation of the Δn (indicated by a typically hysteric P-E loop in ferroelectrics) and thereby a nonvolatile converse magnetoelectric coupling would be enabled.

The above-discussed converse magnetoelectric coupling, enabled through the electrically modulated spin-polarized electron density, in principle exists in all magnetoelectric heterostructures, but is relatively weak compared to the couplings enabled through other mechanisms that will be discussed later. Furthermore, the above-discussed coupling occurs largely within the spin-dependent screening length l_{sc} (typically around 1 nm in ferromagnetic metals[25]). Therefore, to enable a more appreciable change of macroscopic magnetization, the thickness of the constituent magnetic layer should not be significantly larger than l_{sc} such that local magnetic moments across the entire film thickness can be modulated.

Electric field modulated degree of interfacial oxidation. When the dielectric layer is a good solid-state ion conductor (i.e., such as gadolinium oxides[26–29] and MgO with high ionic defect concentrations)[30–32] and when the magnetic layer is an ultrathin ferromagnetic metal (e.g., Fe,[30, 31] Co,[26–29] or Fe$_{0.9}$Co$_{0.1}$[32]) that shows a perpendicular magnetic anisotropy (PMA), experiments have shown that the converse magnetoelectric coupling is significantly larger than the above-mentioned coupling through electric field modulation of electron density. Furthermore, the converse magnetoelectric coupling can become even larger when applying a voltage for a longer time[28] or/and at a higher temperature.[27]

Overall, current fundamental understanding of these experimental observations is largely qualitative. In the case of a Co/gadolinium-oxide system,[26–29] it was proposed that the coupling is enabled through a voltage modulation of the surface oxygen vacancy concentration of the dielectric (see Fig. 2c) and thereby the degree of interfacial Co oxidation. The latter can significantly influence the PMA. For example, experiments performed in a similar Co/AlO$_x$ system[33, 34] have shown that the PMA of the Co film is likely to originate from the presence of a CoO$_x$ layer at the interface. In the section 'Fundamental understanding of Magnetoelectric coupling", we will briefly discuss how DFT modeling can be utilized to gain insights between the degree of interfacial oxidation and the PMA along with the challenges. Other fundamental questions regarding this mechanism will be discussed in the section 'Remaining questions'. From an application perspective, the speed (mainly depending on how fast the ions migrate) and the endurance (repeated oxygen vacancy transport may accelerate dielectric degradation) of the voltage-modulated

magnetism in magnetic/solid-state-ion-conductor heterostructures are both open questions.

Strain-mediated electric field modulation of magnetism. When the dielectric layer is a piezoelectric, electric-field-induced strain can be transferred to the magnetic layer across the interface and modulate magnetism via magnetoelastic coupling. As seen from Fig. 2d, such strain-mediated coupling is not limited to interface, because a strain wave may propagate through the entire magnet. Phenomenological theories have been developed to quantitatively understand the influence of strain[35] and the influence of coexisting strain and surface charges[36] on magnetic anisotropy. Furthermore, employing a ferroelectric may result in a larger piezostrain via ferroelastic switching (i.e., non-180° polarization switching)[37, 38] or structural phase transition.[39–43] A controllable ferroelastic switching, however, is much more difficult to achieve. Phase-field models have been developed to understand how ferroelastic switching in ferroelectrics influences the magnetic domain switching[44] and magnetic domain-wall motion[45] in an overlaid magnet. Detailed discussions on such strain-mediated converse magnetoelectric coupling can be found in a recent review.[12]

Experimental studies on such strain transfer mediated converse magnetoelectric coupling are extensive, and the strength of such coupling can be strong, e.g., a strain-generated effective magnetic field exceedng 3000 Oe has been observed in some magnetoelectric heterostructures.[46] However, a strain typically cannot switch the polarity of a magnetization vector by 180° because a strain cannot break the time-reversal symmetry. Likewise, it is difficult to achieve an electric-field-driven 180° magnetization switching through the modulation of spin-polarized charge densities or interfacial oxidation. Nevertheless, several routes to achieve such electric-field-driven 180° magnetization switching have recently been proposed through computational modeling, as will be discussed later.

Electric field modulated exchange coupling. When the ferroelectric layer also possesses an antiferromagnetic (AF) order coupled to the electric polarization, e.g., in BiFeO$_3$,[47–49] YMnO$_3$,[50] and LuMnO$_3$,[51] one can electrically control the exchange coupling between the AF and ferromagnetic order by rotating the electric polarization, and hence controlling the magnetism (see Fig. 2e). However, the microscopic origins of how an electric field controls the AF order and the exchange coupling cannot be conclusively inferred from these experiments,[47–51] and may vary from material to material. For example, in BiFeO$_3$ thin films, first-principles DFT calculations[52] have shown that the polarization $\boldsymbol{P}$, AF vector $\boldsymbol{L}$ (= $\boldsymbol{M}_{Fe1} - \boldsymbol{M}_{Fe2}$, the difference of two sublattice magnetizations), and the canted magnetization $\boldsymbol{M}_c$ (= $\boldsymbol{M}_{Fe1} + \boldsymbol{M}_{Fe2}$) are mutually perpendicular. Thus, electrically switching the polarization can switch the $\boldsymbol{M}_c$ and further modulate the exchange interaction between the $\boldsymbol{M}_c$ and the magnetization at the bottom surface of an overlaying magnet. This scheme has been utilized to explain the experimental observation of room temperature electric-field-driven 180° net magnetization reversal in a heterostructure consisting of polycrystalline Co$_{0.9}$Fe$_{0.1}$ films deposited on two-domain-variant epitaxial BiFeO$_3$ films,[49] but has not been directly observed by experiments. Furthermore, since BiFeO$_3$ is ferroelastic, strain effect cannot be excluded.[53] In hexagonal LuMnO$_3$ bulk crystals that exhibit AF domain walls clamped at the center of ferroelectric domain walls to reduce free energy,[54, 55] electrically reversing the sign of exchange bias (shown as a shift of the magnetic hysteresis loop) between the LuMnO$_3$ crystal and an overlaying magnet has been experimentally observed at 5 K in the presence of a static magnetic field.[51] This observation has been explained[51] by an exchange bias-mediated scheme as follows. First, an electric field induced ferroelectric domain wall motion can temporarily decouple the AF and ferroelectric domain walls.

npj

Understanding and designing magnetoelectric heterostructures
J-M Hu et al.

4

Second, when the AF and ferroeleric domain walls become clamped once again after the voltage is turned off, the polarity of the uncompensated magnetic moment of the AF domain walls M_{AF}, which determines the sign of the exchange bias, can be reversed by the static magnetic field. Note that this scheme was proposed purely based on macroscopic experimental observations (measuring the magnetic hysteresis loop) without corroboration from either microscopic/mesoscopic experimental observation or computation. Also note that the strain effect can be excluded because $LuMnO_3$ is not ferroelastic (i.e., with only 180° ferroelectric domain walls).

The converse magnetoelectric coupling enabled through the electric field modulated exchange coupling has also been observed in magnetoelectric heterostructures using Cr_2O_3, a magnetoelectric antiferromagnet with no ferroelectricity. Specifically, in a heterostructure consisting of a perpendicularly magnetized Pd/Co multilayer deposited on the (0001) surface of a single-AF-domain Cr_2O_3 bulk singe crystal, electrically reversing the sign of exchange bias has been experimentally observed at 303 K in the presence of a static magnetic field.[56] This observation was explained by arguing that the electrically driven reversal of the singe AF domain reverses the magnetic moment on the Cr_2O_3 surface and thereby the sign of perpendicular exchange bias. Later, in a (0001)-oriented Cr_2O_3 epitaxial film cooled to 223 K under zero magnetic and electric fields, a multi-domain surface magnetization pattern has been directly observed using photo-emission electron microscopy (PEEM) with X-ray magnetic circular dichroism (XMCD) contrast.[57] Notably, such multi-domain surface magnetization patterns can transform into a nearly single-domain state after cooling the film to 223 K under an applied electric field, which supports the proposed scheme of electrically reversed surface magnetization.

It is worth noting that exchange coupling is generally weak. Specifically, the magnitude of the exchange coupling field H_E in $Co_{0.9}Fe_{0.1}/BiFeO_3$ heterostructures, which possibly arises from the exchange interaction between the canted magnetic moment on the $BiFeO_3$ surface and the local magnetic moment at the bottom surface of $Co_{0.9}Fe_{0.1}$, has been shown to range from 50 to 100 Oe by recent experiments.[58, 59] The magnitude of the exchange bias field H_{EB} in heterostructures integrating magnetic layers with $RMnO_3$ ($R = Y$, Lu) or Cr_2O_3 ranges from 60 to 130 Oe, whereas a strain-generated effective magnetic field can be more than 3000 Oe as mentioned above. Note that the exchange coupling-mediated converse magnetoelectric coupling largely occurs within the exchange length l_{ex} (typically below 10 nm, see ref. 60). Therefore, to enable a more significant change in macroscopic magnetization, the thickness of the overlaying magnet typically needs to be smaller than l_{ex} such that local magnetic moments across the entire thickness can be subjected to the same H_E or H_{EB}.

Fundamental understanding of magnetoelectric coupling

Computational modeling can be utilized to understand experimental observations and measurements at multiple temporal and spatial scales. It can also be employed to predict the electronic structure, atomic structure, domain structure, microstructure, and the distributions of fields (e.g., electric/magnetic/stress/temperature field) in a material as well as their kinetic evolution. This will enable physical understanding of an observation or measurement. Below we discuss three examples demonstrating the applicability of computational modeling in understanding the magnetoelectic coupling mechanism(s), and optimizing the strength of magnetoelectric coupling in magnetoelectric heterostructures.

Unraveling the microscopic picture of charge-mediated magnetoelectric coupling using DFT. The first example is the utilization of first-principles DFT calculations to understand the microscopic origins of converse magnetoelectric coupling enabled through electric field modulation of spin-polarized charge densities. Such charge-mediated coupling was first demonstrated experimentally in thin-film magnetic semiconductors, e.g., 5-nm-thick $(In_{0.97}Mn_{0.03})As$.[61] The Curie temperature (T_c) of these magnetic semiconductors depends on the electron hole concentration and therefore can be modulated by an electric field. It was then experimentally demonstrated in thin-film magnetic metals, $L1_0$-ordered FePt (2-nm-thick) and FePd (2-nm-thick), which are immersed in a liquid electrolyte.[62] The first observation of charge-mediated magnetoelectric coupling in magnetoelectric heterostructures was made by Maruyama et al.,[63] who observed an appreciable voltage-controlled magnetic anisotropy in an ultrathin (0.48-nm-thick) ferromagnetic Fe film sandwiched between Au and MgO.

As mentioned above, electrically induced change in the interface magnetic moment Δm in magnetoelectric heterostructures is related to the change in both the interface charge densities $\Delta\sigma$ and the interface spin polarization under the electric field η by $\Delta m = (\Delta n \eta \mu_B)/e$. The quantitative relationship between an applied electric field E and the Δn (or η), however, is difficult to obtain experimentally or analytically. DFT calculations can be utilized to calculate the LDOS with and without an applied electric field (as sketched in Fig. 2b, see an example of such calculation in ref. 64), through which $\Delta\eta$ can be directly obtained. Based on the calculated shift in Fermi level, Δn can be obtained. The term $\Delta n \eta$ is typically known as induced spin density that appears in many computational works (see for example refs 21, 22, 65). As one example, Fig. 3a shows an electric-field-induced accumulation of spin densities at a stoichiometric Fe/MgO interface calculated by DFT calculations.[65] Figure 3b shows the variations of the magnetic moment of the interfacial Fe atom and the magnetocrystalline anisotropy energy (MAE) of the Fe/MgO interface (calculated as the total energy difference for magnetization oriented along an in-
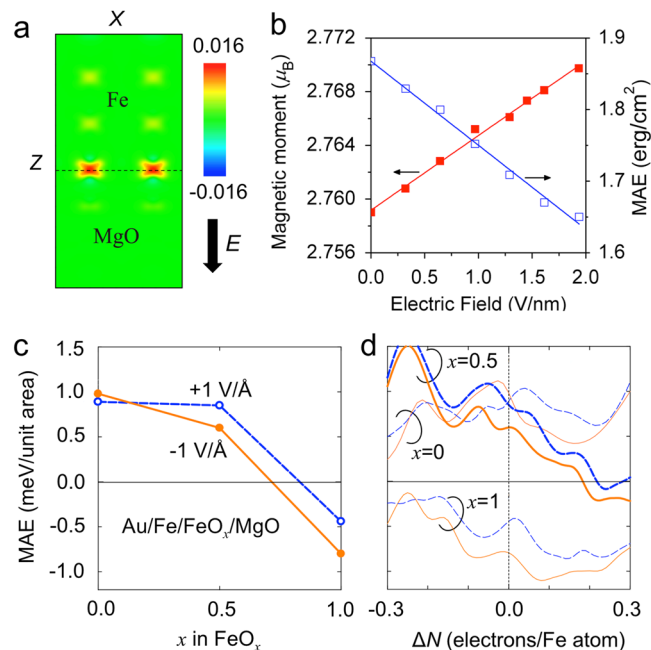

Fig. 3 **a** xz-plane distribution of electrically induced spin densities (in the unit of $e/Å^3$) across a Fe/MgO interface under an electric field of 1 V/nm in the MgO. **b** Modulating the magnetic moment of the Fe atom at the Fe/MgO interface and the MAE of the Fe/MgO interface with an electric field. Influence of **c**, degree of interfacial oxidation (x in FeO_x), and **d**, doping, on the electric field modulation of MAE. Note that varying valence electrons ΔN is equivalent to modulating x in $Fe_{1-x}Co_x$. **a**, **b** were adapted with permission.[65] **c**, **d** were adapted with permission.[66]

Understanding and designing magnetoelectric heterostructures
J-M Hu et al.

npj

5

plane [100] and out-of-plane [001] magnetization, $E_{[100]}$-$E_{[001]}$ in the presence of spin-orbit coupling) with the magnitude of the applied static electric field. The predicted reduction of MAE is qualitatively consistent with the experimental observed reduction of PMA in Au/Fe/MgO heterostructure[63] as a positive voltage is applied.

The power of DFT calculations is that it allows us to access atomic structures that are not experimentally observed or available, and thereby to design the atomic structure for optimum response or functionality. For example, Nakamura et al.[66] considered an interface structure of Au/Fe/FeO$_x$/MgO, and performed DFT calculations to understand the influence of oxygen concentration x on the electric-modulated MAE. As shown in Fig. 3c, for the oxygen concentrations being investigated ($x = 0$, 0.5, 1), applying an electric field can modulate magnetic anisotropy (with the largest modulation at $x = 1$) but cannot change the sign of MAE to switch the PMA to in-plane or vice versa. The existence of an interfacial FeO layer ($x = 1$), however, leads to a negative MAE that suggests an in-plane magnetic anisotropy. This indicates that modulating the degree of interfacial Fe oxidation can have a more significant influence on the MAE than modulating spin-polarized charge densities (see previous sub-section 'Electric field modulated degree of interfacial oxidation'). In addition to the influence of interface layer oxygen concentration, Nakamura et al.[66] also explored how Co doping into the Fe layer in Au/Fe/FeO$_x$/MgO ($x = 0$, 0.5, 1) influences the electric-field-modulated MAE. The Co doping was modeled by varying the numbers of valence electrons in Fe without explicitly introducing Co atoms in lattice. The calculation results are shown in Fig. 3d, which suggest that there is a small window of valence electron number (Co doping level) that results in the sign change of MAE (perpendicular to in-plane switching of magnetic anisotropy and vice versa) with an electric field when $x = 0.5$. This prediction is consistent with experiments in Au/FeCo/MgO.[67]

Now turn to discussion on the limitations. First, employing DFT calculations to predict the influence of other interface layer oxygen concentrations x can be computationally expensive and sometimes formidable. For example, modeling a 90% oxygen concentration ($x = 0.9$) requires at least 9 oxygen atoms and 1 oxygen vacancy (with 10 different arrangements) along with significant increase in the overall size for the model system. By comparison, modeling $x = 0.5$ may only require 1 oxygen atom and 1 oxygen vacancy, while modeling $x = 1.0$ or 0 corresponds to the case with or without a Fe–O layer. Second, DFT calculations cannot predict the kinetic process of local spin evolution when the interface structure or electron density changes under an applied electric field.

Identifying magnetoelectric coupling mechanisms using mescoscale simulations. Converse magnetoelectric coupling in a magnetoelectric heterostructure may occur through the co-action of two or more different coupling mechanisms (see discussions related to Fig. 2a), but the relative contribution of each responsible coupling mechanism can be difficult to determine experimentally. Computational modeling can be utilized to quantify the contribution of individual coupling mechanism by examining the influence of relevant important parameters such as magnetostriction coefficients, exchange bias fields, and magnetic surface anisotropy coefficients, which are related to the strain-mediated, exchange-coupling-mediated, charge-mediated converse magentoelectric coupling, respectively.[12]

As an example, a magnetic/BiFeO$_3$ heterostructure is considered. Applying a voltage to the BiFeO$_3$ can, on one hand, switch the AF order (and possibly switch the canted magnetic moment at the BiFeO$_3$ surface)[52] and thereby switch the magnetization of the thin overlaying magnetic layer through exchange coupling. On the other hand, it can induce strains through the non-180° ferroelectric domain switching, which can then switch the
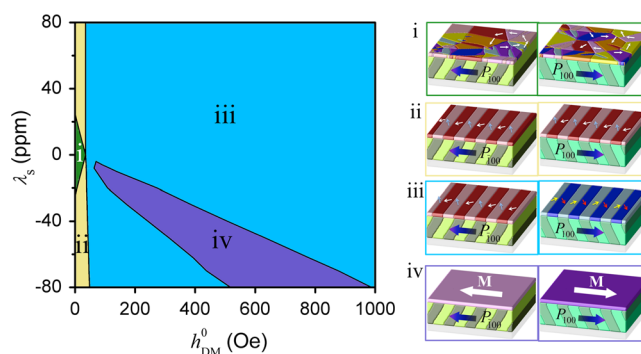

Fig. 4 Diagram showing four different types of electrically driven magnetization switching in magnetic/BiFeO$_3$ heterostructures, including (i) no stripe domain, (ii) domain pattern exchange, (iii) net magnetization reversal, and (iv) uniform magnetization reversal. The switching type depends on the magnitude of Dzyaloshinskii–Moriya interaction (h_{DM}^0) and the saturation magnetostriction (λ_s). Shown on the right are the typical magnetic and ferroelectric domain structures before and after electrically switching the in-plane polarization (P_{100}) in the BiFeO$_3$ layer. The arrows indicate local magnetization directions. Adapted with permission.[71]

magnetization in the overlaying magnet through the magnetoelastic coupling. It is worth noting that, for most of the thin-film magnetic materials, the strain effect is not negligible, especially given the fact that the magnetoelastic coupling in relatively thin films (e.g., <5 nm for polycrystalline Ni and NiFe films)[68] can be significantly enhanced compared to their bulk counterparts. Therefore, for the observed electrically driven net magnetization reversal in magnetic/BiFeO$_3$ heterostructures,[49, 69] the effects of exchange coupling and strain coexist.[70]

To computationally evaluate the contributions of these two effects during an electrically driven magnetization switching, a diagram of magnetization switching type has been established[71] using phase-field simulations (see Fig. 4) for a representative heterostructure of Co$_{0.9}$Fe$_{0.1}$/BiFeO$_3$. The *horizontal axis* represents the magnitude of the effective magnetic field possibly produced by the canted magnetic moment[52] on the BiFeO$_3$ film surface, which originates from the Dzyaloshinskii-Moriya-type asymmetric exchange interaction.[72, 73] The *vertical axis* represents the saturation magnetostriction (λ_s) of the 2.5-nm-thick polycrystalline Co$_{0.9}$Fe$_{0.1}$ film. Note that the (001)$_p$-oriented BiFeO$_3$ film has two variants of ferroelastic domains with 71° domain walls due to the biaxial anisotropic strains from the (110)-oriented DyScO$_3$ substrate.[49, 69] In the phase-field model, the thickness of the BiFeO$_3$ film is assumed to be about 110 nm (thicker than the critical thickness, about 70 nm,[74] for the formation of interface dislocations) to permit partial release of substrate clamping. This would enable freely deformed lattices in the top few atomic layers of the BiFeO$_3$, and two-variant striped ferroelastic domains on the BiFeO$_3$ film surface.

As shown in Fig. 4, Co$_{0.9}$Fe$_{0.1}$ and BiFeO$_3$ can both exhibit a two-variant stripe domain structure with one-to-one match in local domain patterns (consistent with experimental observations)[49, 69], providing that at least one of the two parameters (λ_s or h_{DM}^0) is sufficiently large. This indicates that both the local elastic coupling and local exchange coupling can stabilize locally coupled magnetic and ferroelectric domains across the interface. However, the electrically driven reversal of net magnetization in the Co$_{0.9}$Fe$_{0.1}$ film (phase iii in Fig. 4, which has been demonstrated experimentally)[69] only occurs when h_{DM}^0 is larger than a threshold value (35–50 Oe), otherwise a pattern exchange among neighboring domains (phase ii) would be an energetically favorable option. The simulations also predicted a possible uniform magnetization reversal (phase iv) when free energy contributions from the

npj

Understanding and designing magnetoelectric heterostructures
J-M Hu et al.

6

surface electro-strain and surface exchange-coupling field are comparable. Therefore, it is the modulation of exchange coupling that dominates the electrically driven (net or uniform) magnetization reversal in the present magnetic/$BiFeO_3$ heterostructure.

Optimizing macroscopic effective magnetoelectric coupling coefficient. Computational screening of the optimum size, shape, topology of a macroscopic structure for a desirable property or a set of desirable properties (i.e., structural optimization) is a well-established methodology in engineering design.[75] For example, computers can find the optimum hole size (the design variable) of a load-bearing flywheel that leads to minimum weight (the property, or objection function) under the condition that the peak stress is below a threshold value (constraint). Recent advances in computational screening of the optimum crystal atomic structure for a desirable property[76] represent the microscopic analog of such an optimization problem. At the mesoscale, one can evaluate the effective material properties of a given microstructure through, for example, computational homogenization[77] (which typically applies best to materials with periodic structures) and effective medium theories.[78] However, the inverse problem of identifying the optimum materials microstructure for desirable properties is more challenging mainly due to the complexity of the microstructure data. Such microstructural optimization bridges the gap between the macroscopic structural optimization and the microscopic atomic structure optimization, thus is critically important for the entire hierarchy of computational materials design.[79]

In the field of magnetoelectric heterostructures, effective magnetoelectric coupling coefficients have been evaluated or predicted by effective medium theories,[80, 81] thermodynamic theories,[82, 83] micromechanical models (see for example refs 84, 85 and a comprehensive literature survey in ref. 86), homogenization methods,[87, 88] and by phase-field simulations.[89–94] Note that phase-field method can predict the co-evolution of the microstructure (grain/domain structure) and its corresponding effective (linear[89, 92] and nonlinear)[90, 91, 93, 94] magnetoelectric coupling coefficients under externally applied fields. Notably, Ni et al.[89] proposed a phase-field method to identify the optimum phase morphology in piezomagnetic-piezoelectric composites that lead to a maximum linear direct magnetoelectric coupling coefficient.

Predicting new types of magnetoelectric coupling
Predictive computational modeling is a key component in computational materials design. A predictive model is typically established based on our fundamental understanding of the physics and chemistry of a system, and can generate data from which a statistically correct predictive model may be established through machine learning. A statistically correct predictive model can produce the desirable outcomes much more quickly than computations based on a physical or chemical model especially when the system size is large, and thus may accelerate materials discovery. In fact, using machine learning to discover statistically correct predictive model from quantum computations data has been explored since the year 2003.[95–103] Furthermore, a statistically correct predictive model can also be discovered from high-quality experimental data. More discussions of such data-driven computational materials design (the *bottom layer* in Fig. 1) will be given in the last section of this paper. In the present section, we will discuss three examples showing how computation-based physical models have been utilized to predict new types of magnetoelectric coupling in a magnetoelectric heterostructure.

Magnetoelectric coupling via polarization-reversal controlled interface chemical bonding. Electrically reversing the spontaneous polarization in a tetragonal $BaTiO_3$ would switch the Ti atoms slightly displaced from the centers of the Ti–O octahedron in one direction to the opposite direction. Using first-principles calculations, Duan et al. first explored how such an ionic displacement influences the magnetism at an Fe/$BaTiO_3$ interface.[104] The most stable (lowest energy) interface structure is identified as a TiO_2-terminated interface with the interface O atoms sitting collinearly above the Fe atoms (see schematic in Fig. 5a that illustrates a $(Fe_2)_9$–TiO_2–$(BaO–TiO_2)_m$ supercell). An upward polarization moves the Ti atom towards the Fe atoms, leading to a shorter Fe–Ti bond length. As a result, the Ti atom in the very first TiO_2 layer neighboring the Fe layer exhibits an enhanced magnetic moment, as shown in the left image in Fig. 5b. Conversely, a downward polarization displaces the Ti atoms away from the Fe atoms. The longer Fe–Ti bond length reduces the magnetic moment of the Ti atom (see the *right image* in Fig. 5b).

These predictions were corroborated by later experimental observations.[105, 106] Firstly, in an ultrathin $BaTiO_3$ film grown on a
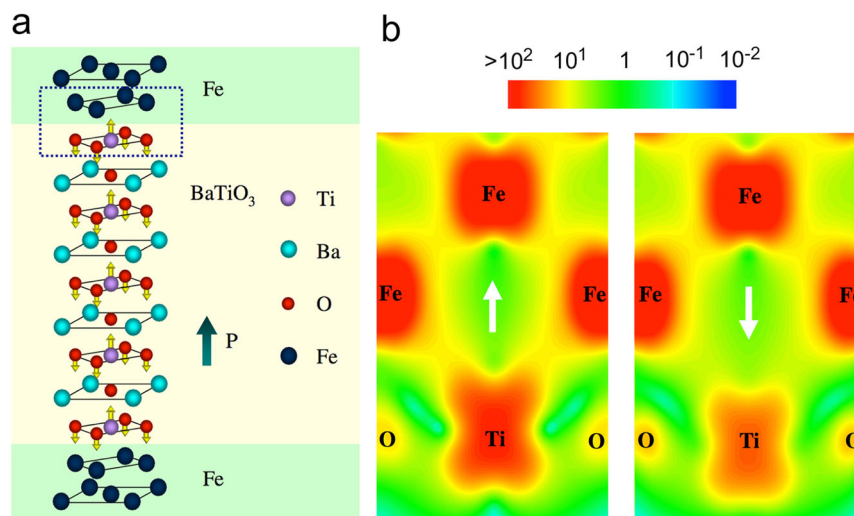

Fig. 5 a Atomic structure of the Fe/$BaTiO_3$/Fe multilayer with a super cell of $(Fe_2)_9$–TiO_2–$(BaO–TiO_2)_4$, in which the *arrows* schematically indicate the displacements of the Ti and O atoms. **b** The calculated minority spin densities (in arbitrary unit) at the upper Fe/$BaTiO_3$ interface (marked by *dashed rectangular* in **a**). Adapted with permission.[104]
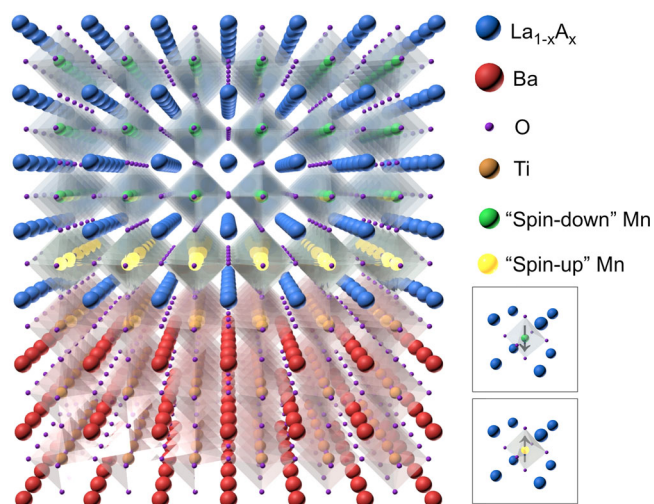
Understanding and designing magnetoelectric heterostructures
J-M Hu et al.

np[j]

7

Fig. 6 Schematic of an electrically driven interface magnetic phase transition in a $(La_{1-x}A_x)MnO_3/BaTiO_3$ interface. Electrically reversing the electric polarization in the $BaTiO_3$ layer can switch the magnetic moment of the interface Mn atoms by 180°, resulting in a ferromagnetic to AF phase transition occurring only at the interface. The oxygen octahedral rotations in these perovskite materials are not shown for simplicity. This mechanism was first predicted by Burton et al.[112]

Fe(001) single crystal, the predicted Fe–TiO_2–BaO–TiO_2 interface structure was confirmed experimentally by Meyerheim et al.[105] Secondly, in a Fe/$BaTiO_3$/$(La_{2/3}Sr_{1/3})MnO_3$ all-film heterostructure, the atomically resolved scanning transmission electron microscope image of the Fe/$BaTiO_3$ interface suggests a possible Fe–FeO–TiO_2–BaO–TiO_2 interface structure.[106] Although such interface structure may be different from the prediction, X-ray resonant magnetic scattering measurements indicate that appreciable magnetic moments arise from the interfacial Ti and O atoms.[106]

In the case of such interface bonding mediated magnetoelectric coupling, the change of magnetic signals arises mainly from one or two atomic layers at the interface. Furthermore, this mechanism requires the use of ferroelectric oxides where ferroelectricity is due to the off-center shift of the transition metal cation, e.g., $BaTiO_3$,[105–107] $Pb(Zr_{0.2}Ti_{0.8})O_3$,[108] and $PbTiO_3$.[109] By comparison, magnetoelectric coupling enabled through electrically modulated spin-polarized charge densities (all dielectric materials are in principle applicable, see Fig. 2a) is less sensitive to the details of interface bonding configuration, and has an effective length typically on the order of the spin-dependent screening length (l_{sc}) of the magnet.

Magnetoelectric coupling via electrically induced interface magnetic phase transitions. This type of magnetoelectric coupling is based on the electrically induced ferromagnetic-to-AF phase transition that occurs strictly within one or two monolayers of the magnetic layer at the magnetic/ferroelectric interface[110–114] (see schematic in Fig. 6). Thus it is different from existing reports of electrically shifting the critical temperatures of bulk magnetic phase transitions in magnetoelectric heterostructures. These bulk magnetic phase transitions include ferromagnetic-paramagnetic transitions (that is, electrically tuning Curie Temperature),[61, 115–121] superparamagnetic-ferromagnetic transitions (electrically tuning Blocking temperature),[122] electronic phase separations,[123] and Verwey transitions.[124] Table 1 summarizes a partial list of existing reports[61, 110–124] on the electric-field control of magnetic phase transitions in magnetoelectric heterostructures.

Burton and Tsymbal[112] first predicted, through first-principles calculations, such magnetoelectric coupling at the interface of a doped manganite, $La_{1-x}A_xMnO_3$ (LAMO, A = Ca, Sr, Ba), and a $BaTiO_3$ ferroelectric. It is commonly accepted that magnetic phase states and electronic behaviors of LAMO are sensitive to the electron hole concentration. Such carrier concentration can be controlled through chemical doping and electric-field effect. Given that the depletion/accumulation of polarization charges can electrostatically modulate the electron hole concentration in the adjacent LAMO across the interface, it is possible to electrically toggle the interface magnetic phase state between two ground states that have similar energy levels.

Such an electrically induced interface magnetic phase transition has been successfully utilized to interpret the polarization-reversal-induced change in the atomic magnetic moment of Mn^{x+} in a $La_{0.8}Sr_{0.2}MnO_3/Pb(Zr_{0.2}Ti_{0.8})O_3$ heterostructure.[110] It is also predicted[113] that at such an interface magnetic phase transition can yield an enhanced tunneling electroresistance (i.e., polarization-reversal induced change of electric resistance in an ultrathin ferroelectric capacitor). Recently, enhanced tunneling electroresistance has been experimentally observed by Yin et al.[114] in a $La_{0.7}Sr_{0.3}MnO_3/BaTiO_3/La_{0.5}Ca_{0.5}MnO_3/La_{0.7}Sr_{0.3}MnO_3$ heterostructure. This observation further substantiates the proposed mechanism of an interface magnetic phase transition. More recently, in a Fe/$BaTiO_3$ heterostructure with an oxidized interface (that is, Fe–FeO_x–TiO_2–BaO), Radaelli et al.[111] experimentally demonstrated that polarization reversal can suppress or restore the magnetization of the interfacial FeO_x layer, while barely affects the magnetization in the bulk region of Fe. To our knowledge, this is so far the most direct evidence for an electrically induced interface magnetic phase transition.

Searching for new magnetoelectric coupling in superlattices. Rationally designed superlattices can also enable the discovery of new types of magnetoelectric coupling.[125–128] For example, in superlattices of cation ordered perovskites $(ABO_3)_1/(A'BO_3)_1$ that exhibit antiferroelectric displacements in both of the constituting layers, Rondinelli and Fennie[125] used DFT calculations to reveal an octahedral-tilt induced spontaneous polarization. Because the octahedral tilt is also coupled with magnetization in perovskites,[129] Rondinelli and Fennie envisaged that the polarization can be coupled with magnetization through the octahedral tilt in such perovskites superlattices. This prediction is supported by a recent work by Xu et al.,[126] who demonstrated an electric-field-driven magnetization switching in a $(BiFeO_3)_1/(NdFeO_3)_1$ superlattice using effective Hamiltonian calculations.

Furthermore, Puggioni et al.[127] predicted the coexistence of ferroelectricity and magnetism in a $(LiOsO_3)_1/(LiNbO_3)_1$ superlattice through a combination of DFT calculations and dynamic mean-field theory. The superlattice geometry can enhance the degree of electron-electron correlation in a nonmagnetic polar metal ($LiOsO_3$ here) to an extent that the polar metal would transform into an insulator through Mott transitions, leading to the emergence of a robust ferroelectric polarization. The enhanced electron-electron correlation also localizes electron spins such that magnetic ordering appears. It will be interesting to quantitatively investigate the magnetoelectric coupling in this system and polar metals[130] in general.

Most recently, Mundy et al.[128] experimentally discovered the coexistence of ferroelectricity and magnetism at room temperature in a $(LuFeO_3)_9/(LuFe_2O_4)_1$ superlattice. The principle is to drive the ferrimagnetic $LuFe_2O_4$ into a simultaneously ferroelectric state through the rumpling (specifically, trimer lutetium distortions, which can be seen from high-resolution electron microscopy images) imposed by neighboring $LuFeO_3$. This principle is supported by two facts predicted from DFT calculations. First, the $LuFe_2O_4$ exhibits an antiferroelectric ground state and a ferroelectric metastable state exhibiting a slightly higher energy. Second, the rumpling is only allowed in the ferroelectric state. Of particular interest, a significant electric field control of

npj

Understanding and designing magnetoelectric heterostructures
J-M Hu et al.

8

Table 1. Some experiments (Exper.) and computations (Comput.) on magnetoelectric coupling via electrically controlled magnetic phase transitions in horizontal magnetoelectric heterostructures

Heterostructure	Electrically Controlled Phenomenon	Mechanism	Note	Ref.
Electrode/Pb($Zr_{0.2}Ti_{0.8}$)O_3/(La$_{0.7}$Ca$_{0.3}$)MnO$_3$ (50)	Electronic Phase Separation	Charge Screening	Exper. (Electron Transport)	[123]
Metal/Insulator/(In$_{0.97}$Mn$_{0.03}$)As (5)	Curie Temperature	Charge Screening	Exper. (Hall Transport)	[61]
0.67PMN-0.33PT (001)/La$_{0.75}$Ca$_{0.25}$MnO$_3$ (25~75)	Curie Temperature	Mainly Strain	Exper. (Electron Transport)	[115]
0.72PMN-0.28PT (001)/La$_{0.7}$A$_{0.3}$MnO$_3$ (20~50), A=Sr, Ca	Curie Temperature	Mainly Strain	Exper. (Magnetization v.s. Temperature)	[116]
SrTiO$_3$/La$_{0.7}$Sr$_{0.3}$MnO$_3$ (~2.7)/SrTiO$_3$	Curie Temperature	Charge Screening	Exper. (Magneto-Transport)	[117]
Au/P(VDF-TrFE)/(Ga$_{0.94}$Mn$_{0.06}$)As (7)	Curie Temperature	Charge Screening	Exper. (Hall Transport)	[118]
Au/Ionic Liquids/La$_{0.8}$Ca$_{0.2}$MnO$_3$ (5)/SrTiO$_3$	Curie Temperature	Charge Screening	Exper. (Electron Transport)	[119]
Au/Cr/HfO$_2$/Co(0.4)	Curie Temperature	Charge Screening	Exper. (Hall Transport)	[120]
0.68PMN-0.32PT (001)/SrTiO$_3$/La$_{0.7}$Ca$_{0.3}$MnO$_3$ (30)	Curie Temperature	Mainly Strain	Exper. (Electron Transport)	[121]
0.68PMN-0.32PT (011)/Ni-NPs (16-nm-diameter)	Blocking Temperature	Strain	Exper. (Magnetization v.s. Temperature)	[122]
0.71PMN-0.29PT (011)/Fe$_3$O$_4$ (55)	Verwey MIT	Strain	Exper. (Electron Transport)	[124]
BaTiO$_3$/Fe (1)	IMPT (in the interface FeO layer)	Ionic Displacement	Exper. (XMCD) and Comput. (DFT+U)	[111]
BTO/La$_{0.5}$A$_{0.5}$MnO$_3$ (A=Ca, Sr, Ba)	IMPT	Charge Screening	Comput. (DFT+U)	[112]
Pb($Zr_{0.2}Ti_{0.8}$)O_3/La$_{0.8}$Sr$_{0.2}$MnO$_3$ (4)	IMPT	Charge Screening	Exper.(MOKE, XANES)	[110]
La$_{0.7}$Sr$_{0.3}$MnO$_3$/BTO/La$_{0.6}$Sr$_{0.4}$MnO$_3$	IMPT (in La$_{0.6}$Sr$_{0.4}$MnO$_3$)	Charge Screening	Comput. (DFT+U)	[113]
La$_{0.7}$Sr$_{0.3}$MnO$_3$/BTO/La$_{0.5}$Ca$_{0.5}$MnO$_3$/ La$_{0.7}$Sr$_{0.3}$MnO$_3$	IMPT (in La$_{0.5}$Ca$_{0.5}$MnO$_3$)	Charge Screening	Exper. (Electron Transport) and Comput. (DFT+U)	[114]

The thickness of the magnetic layer is indicated (in the unit of nanometer) for experimental works
NPs Nanoparticles, *MIT* metal-insulator-transition, *IMPT* interface magnetic phase transition (ferromagnetic-antiferromagnetic transition herein), *XMCD* X-ray magnetic circular dichroism, *MOKE* magneto-optical Kerr effect, *XANES* X-ray absorption near edge spectroscopy

ferrimagnetism has been observed in this (LuFeO$_3$)$_9$/(LuFe$_2$O$_4$)$_1$ superlattice at 200 K: an up and down ferroelectric domain pattern (written through a nanoscale electric probe in an atomic force microscope) can induce an identical magnetic domain pattern (observed at zero magnetic field through XMCD-PEEM). This intriguing experimental observation may stimulate more computational works of exploring magnetoelectricity in superlattices.

Designing magnetoelectric heterostructures for optimum device performances

In this section, we will discuss how computational modeling tools such as phase-field method can be utilized to optimize the performances of a magnetoelectric device prototype by designing the magnetoelectric heterostructures.

Design for electric-field-driven 180° magnetization switching. In magnetoelectric random access memories (MeRAM, see a relatively comprehensive literature survey in ref. 12), a magnetization vector is switched with an electric field rather than a current, thus dissipating much less energy. A 180° magnetization switching is common in conventional magnetoeresistive random access memories but challenging in MeRAM, because applying a time-invariant electric field cannot break the symmetry and usually leads to an at most 90° magnetization switching. If a MeRAM

element integrates a magnetoresistive multilayer such as a magnetic tunnel junction, a 90° switching will only yield approximately half of the maximum resistance change[131] and therefore relatively small signal-to-noise ratio. It is therefore imperative to achieve a full 180° magnetization switching in MeRAM elements to make the latter more competitive among all emergent technologies of random access memories.

There exist experimental reports of achieving electrically driven 180° magnetization reversal in a MeRAM element by simultaneously utilizing an ultrafast electric-field pulse and a static magnetic field,[132, 133] or a 180° net magnetization reversal in a MeRAM element based on a two-domain-variant BiFeO$_3$ film.[49] However, a purely electric-field-driven 180° magnetization switching has not yet been experimentally demonstrated. Below we will briefly discuss three different computationally designed approaches towards this goal. Note that these approaches are based on a rational design of the size, shape, and control conditions of magnetoelectric heterostructures. They do not invoke any new magnetoelectric coupling mechanisms beyond those discussed in last section.

The first approach exploits the charge-mediated electric field control of interlayer exchange coupling (IEC) in a ferromagnetic/non-magnetic/ferromagnetic trilayer on a ferroelectric underlayer (see schematic in Fig. 7a). It is well accepted that the IEC can be switched between a ferromagnetic type (parallel magnetization

Understanding and designing magnetoelectric heterostructures
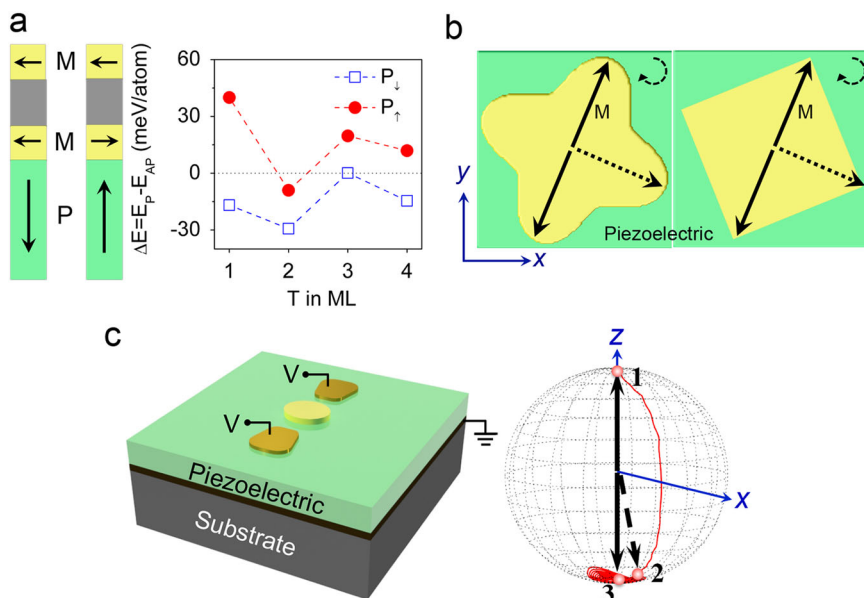J-M Hu et al.

npj

9

Fig. 7 **a** Reversing polarization in a ferroelectric layer may change the type of interlayer exchange coupling in adjacent ferromagnetic/non-magnetic/ferromagnetic trilayer mediated by charge densities, demonstrated by first-principles calculation of the energy density difference between the parallel (ferromagnetic) type and the antiparallel (AF) type in a $PbTiO_3/Fe_1/Au_T/Fe_1$ heterostructure. Reproduced with permission.[109] Strain-mediated electric-field-driven 180° magnetization switching in **b** a flower-shaped or a square-shaped nanomagnet fabricated on a piezoelectric bottom layer (substrate or film) via two consecutive 90° magnetization switching (see the arrows), adapted with permission,[138, 139] and **c** an elliptic cylindrical nanomagnet on a piezoelectric film via precessional magnetization switching (see one possible spatial magnetization trajectory on the *right*), adapted with permission.[145]

configuration) and an AF type (antiparallel) by tuning the thickness of the non-magnetic space layer.[134] Fechner et al.[109] explored the possibility of using an electric field to toggle the IEC type via polarization-reversal controlled interface chemical bonding. Using a $PbTiO_3/Fe_1/Au_T/Fe_1$ heterostructure as an example (where subscript 'T' indicates the number of monolayers), their first-principle calculations indicate that the electric-field-induced polarization reversal can transform the IEC type when $T = 1$ and 4 (see plot in Fig. 7a). Such a transformation of IEC type should lead to a purely electric-field-driven 180° magnetization switching in the Fe monolayer adjacent to the $PbTiO_3$. An earlier report by Zhuravlev et al.[135] exploited a similar approach to achieve electrically controlled IEC in a ferromagnetic/ferroelectric/ferromagnetic trilayer.

The second approach is based on the strain-mediated electric field control of magnetism in a geometrically engineered nanomagnet fabricated on a piezoelectric layer. It has been theoretically demonstrated that applying a suitable sequence of uniaxial normal strain near the pre-existing magnetic easy axis of a single-domain magnet can rotate the magnetization vector in a deterministic manner and achieve a 180° magnetization switching.[136, 137] However, these proposals rely on the use of either a rotating piezostrain,[136] or a single-crystal magnet that shows two mutually perpendicular magnetic easy axes due to a four-fold magnetocrystalline anisotropy.[137] Recently, it has been shown that two pre-existing and mutually perpendicular magnetic easy axes can also appear in a flower-shaped magnetic nanodot with a four-fold shape anisotropy,[138] or in a square-shaped magnetic nanodot[139] with a four-fold magnetic configurational anisotropy[140] (see schematic in Fig. 7b). Using micromagnetic phase-field simulations, it was further shown that applying a bipolar[138] or unipolar[139] piezostrain pulse along the y-axis can switch the magnetization by 180° through two consecutive clockwise 90° magnetization switching (see the *arrows* in Fig. 7b). Compared to previous schemes,[136, 137] these geometrical design based schemes enable greater design flexibility such as a wider range of materials selection and readily tunable angle between the applied piezostrain and the pre-exiting magnetic easy axes.

The third approach exploits the dynamics of strain-mediated electrically controlled magnetism. This scheme for the 180° magnetization reversal also occurs in two steps. As an example, we consider a heterostructure consisting of a 1.1-nm-thick elliptical-cylinder-shaped CoFeB magnet with PMA[141] on a piezoelectric thin film (see schematic in Fig. 7c). The first step is to apply a nanosecond-long voltage pulse to the piezoelectric (based on an electrode configuration proposed by Cui et al.,[142] also sketched in Fig. 7c), generating a nanosecond-long pulse of local strain on the piezoelectric film surface that can temporarily rotate the perpendicular magnetic easy axis of the CoFeB to its in-plane long axis. This will induce a precession motion of the upward magnetization vector about the latter (i.e., from point 1 to 2 in Fig. 7c). Note that such local surface strain can rise and fall quickly enough (down to sub-nanosecond according to simulations)[143] to rotate the magnetic easy axis promptly. The second step is to remove the strain when magnetization possesses a negative out-of-plane component. The magnetization will then precess about the re-established perpendicular easy axis before eventually achieving equilibrium along the downward direction via damping (from point 2 to 3 in Fig. 7c). A 180° switching is now completed. Building on previous schemes that involve the use of a static magnetic field,[132, 133, 144] this scheme for purely electrically controlled 180° perpendicular magnetization switching has been first demonstrated by micromagnetic phase-field simulations[145] and then by other computational models.[146, 147] This scheme has also been adapted to realize a purely electric-field-controlled 180° in-plane magnetization switching in a 4-nm-thick CoFeB nanodot.[143]

Design for electric field driven fast magnetic domain-wall motion. Dynamics of magnetic domain-walls is another topic of great technological importance for applications. A familiar example is a magnetic domain-wall racetrack memory,[148] which is based on a current-induced fast magnetic domain-wall motion in a magnetic nanowire. However, it would be much more energy-efficient to drive
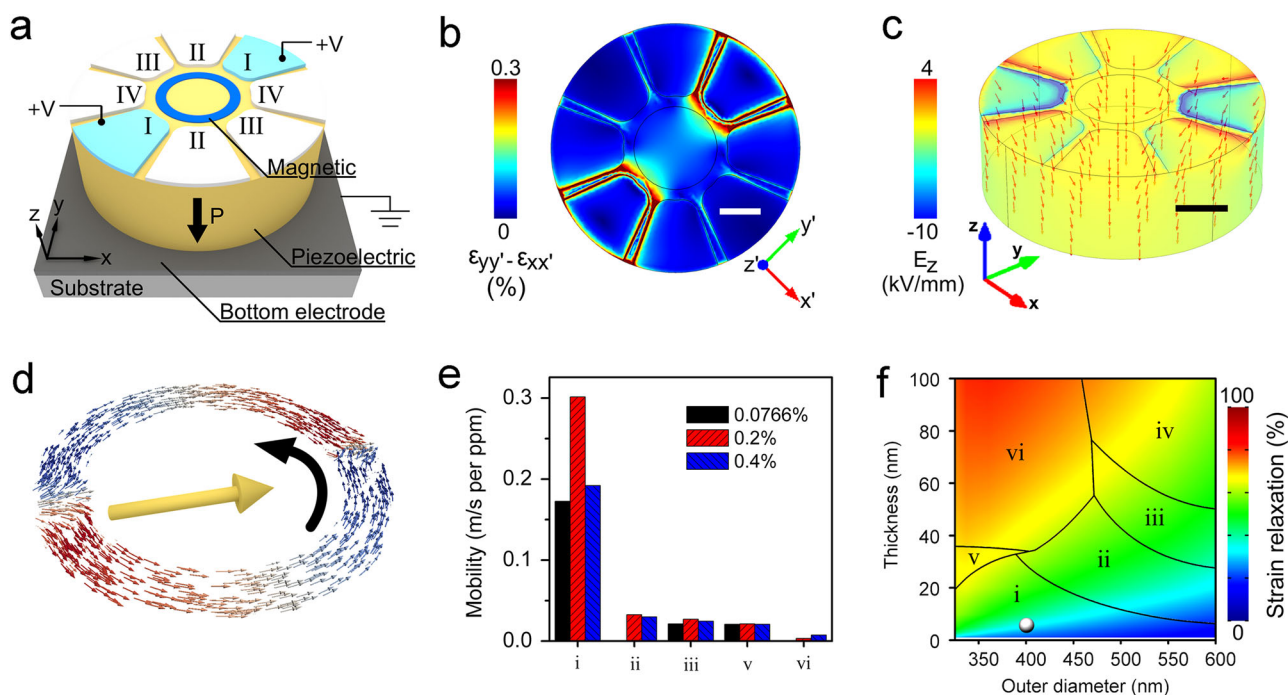
npj

Understanding and designing magnetoelectric heterostructures
J-M Hu et al.

10

Fig. 8 **a–c** Optimizing the top electrodes structure (four pairs in total, see **a**) for maximum surface piezostrain in the *central circle* region (marked in **b**, scale bar = 200 nm) in response to a driving voltage of 1.1 V, under the constraint that maximum local electric fields (see 3-D distribution in **c**, scale bar = 200 nm) would not exceed the dielectric breakdown field. **d–f** Optimizing the domain-wall structure (see a transverse wall structure (type i) in **d**) for maximum strain-controlled domain-wall mobility (results are summarized in **e**) in a ring-shaped nanomagnet, under the constraints that the thermal stability is sufficiently high (>40) and that the degree of strain relaxation in the magnetic nano-ring is sufficiently low (<30%). The dimension of the nano-ring determines the configuration and the thermal stability of domain-wall structure, and the degree of strain relaxation as well, adapted with permission[154]

the motion of magnetic domain-walls with an electric field rather than a current. Electric-field-driven magnetic domain-wall motion has been demonstrated experimentally in a number of magneto-electric heterostructures,[149–152] and computationally in a peculiar heterostructure consisting of a magnetic nanowire sandwiched by a Si bottom substrate and a Pb(Zr,Ti)O$_3$ (PZT) top film.[153] However, none of these reports have demonstrated an average magnetic domain-wall velocity exceeding 100 m/s, a speed comparable to that of current-driven magnetic domain-wall motion.

Recently, a scheme has been proposed[154] to achieve a fast (>100 m/s) electric-field-driven magnetic domain-wall motion by computationally designing the dimension, geometry and control condition of a magnetoelectric heterostructure. Figure 8a shows the key components of the proposed magnetoelectric hetero-structure that comprises of a ring-shaped nanomagnet (amor-phous Co$_{40}$Fe$_{40}$B$_{20}$) grown on top of a piezoelectric disk (polycrystalline PZT). Four pairs of top electrodes and an electrically grounded bottom electrode are utilized to generate uniaxial piezostrains sequentially along the I-I, II-II, III-III, and IV-IV axes. In Fig. 8a, identical voltages of 1.1 V are applied to electrode pair I-I. Figure 8b and 8c present the corresponding top-view distribution of the uniaxial piezostrain ($\varepsilon_p = \varepsilon_{y'y'} - \varepsilon_{x'x'}$) along the I-I axis (y'-axis) and the 3-D electric field distributions, respectively. Further application of identical voltages to electrodes II-II can generate ε_p along the II-II axis, and so on. The shape and dimension of the top electrodes (design variables) have been optimized in such a way that one can get a maximum average piezostrain within the central circle of the PZT surface under a given driving voltage (the objective function of design), under the constraint that the maximum local electric field must be smaller than the dielectric breakdown threshold of PZT film.

According to micromagnetic phase-field simulations, the sequential uniaxial piezostrains along the above-mentioned four axes can drive a unidirectional circulation of two magnetic

domain-walls in the ring magnet, a feature that has potential applications as magnetoelectric memories or motors.[154] Shown in Fig. 8d is a transverse-type magnetic domain-wall structure that possesses the highest strain-controlled magnetic domain-wall mobility (objective function) among all six different types of magnetic domain-wall structures (see Fig. 8e). As further shown in Fig. 8f, engineering the dimension of the ring magnet (design variable) can control the type of domain-wall structure. However, the following two design constraints, both of which are relevant to the ring dimension, need to be imposed during optimization. First, the degree of strain relaxation must be kept at a reasonable low value. Second, the thermal stability of the magnetic domain-wall structure must be sufficiently high.

The white sphere in Fig. 8f marks the ring dimension used in Figs 8a–d. This is an optimum ring dimension (identified via micromagnetic phase-field simulations) that results in high strain-controlled magnetic domain-wall mobility under a low driving voltage. High magnetic domain-wall mobility leads to high domain-wall circulation speeds (up to 500 m/s) and therefore fast device responses. Low driving voltage is important to achieving low energy dissipation. In the present design, the energy dissipation (~0.2 fJ per 180° magnetic domain-wall circuit) is approximately three orders of magnitude smaller than the case using a spin current as the driving stimulus (~0.2 pJ). Table 2 summarizes the design variables, objective functions, and the design constraints used in designing the electrode structure and the dimension of magnetic nano-ring.

It is also worth noting that further optimization of the device performances is possible (i) by varying other design variables, including for example the edge roughness of the ring magnet, the microstructure of the PZT, and the magnetic/piezoelectric inter-face structure; and (ii) by searching for or employing magnetic materials with better magnetoelastic responses and piezoelectric materials with better electromechanical responses.

Understanding and designing magnetoelectric heterostructures
J-M Hu et al.

npj

11

Table 2. Design parameters for the magnetoelectric device prototype based on the voltage-driven magnetic domain-wall motion (see Fig. 8)

Design variables	Objective functions	Behavior constraints
Shape and dimension of electrodes	Piezostrain	Maximum local electric field
Dimension of nanomagnet	Strain-controlled magnetic domain-wall mobility	Degree of strain relaxation, thermal stability of magnetic domain-wall structure

The terminologies in the first row follow those utilized in classical structural optimization problems.[75]

Remaining questions

In above sections, we discussed how computational methods have been utilized to guide the understanding of magnetoelectric coupling mechanisms, the experimental discovery of new types of magnetoelectric coupling, and the design of magnetoelectric heterostructures for achieving optimum device performances. Below we will first discuss some remaining questions concerning magnetoelectric heterostructures. Some of these questions could be addressed by employing a data-driven computational materials design approach. A perspective on this new paradigm will then be given.

Microscopic origins of magnetoelectric coupling mechanisms. Despite extensive experimental and theoretical efforts, a thorough microscopic understanding of the magnetoelectric coupling mechanisms is still lacking. We believe this is one of the two most immediate questions that need to be addressed, which includes at least two aspects as discussed below.

First, several mechanisms have been suggested for the converse magnetoelectric coupling in the Fe/BaTiO$_3$ heterostructure, including the electrically controlled interface chemical bonding,[104] spin-polarized charge densities,[24] interface magnetic phase transition,[111] and strain.[155] In the case of relatively thick magnetic films, both theories[36] and experiments[156, 157] have demonstrated that the strain mechanism should dominate. However, this conclusion was complicated by the observation of strong charge-mediated magnetoeletric coupling by Jedrecy et al.[158] in a bilayer thin-film heterostructure Co (40 nm)/BaTiO$_3$ (17 nm), which was explained using a recent theory proposed by Jia et al.[159] The theory suggests that the effective length of charge-mediated magnetoelectric coupling can reach tens of nanometers in thickness through a spiral arrangement of interfacial spin densities, well transcending the spin-dependent screening length (~1 nm). In the case of ultrathin magnetic films, it remains unclear under what conditions a particular interface-based mechanism would be dominant.

Second, there are at least two fundamental questions regarding the converse magnetoeletric coupling based on electric field modulation of the degree of interfacial oxidation: *How does the interfacial oxide layer influence the magnetic anisotropy of the metal? How to understand the scale of such interfacial-oxidation-mediated converse magnetoelectric coupling?* For the first question, let us consider a Fe/FeO$_x$/MgO interface. As seen from the DFT calculations in Fig. 3c, the degree of Fe oxidation can significantly influence the magnetocrystalline anisotropy because the Fe–O orbit hybridization can significantly alter the d-band occupation.[66] These calculations do not, however, include how the magnetic property of the interfacial FeO$_x$ layer influences the magnetic anisotropy. In fact, the interfacial FeO$_x$ layer was considered to be responsible for the experimental observation of exchange bias at the Fe/MgO interface,[160] and it was also shown that a higher oxygen concentration (x) generates a larger exchange bias.[160] Thus, electrically modulating the degree of interfacial oxidation may alter magnetic anisotropy through the modulation of d-band structure or/and exchange bias. But it still remains unclear whether both mechanisms (interfacial oxidation and exchange coupling) coexist, and if so, what would be the weight of these two mechanisms. DFT calculations of the interface spin structure under different degrees of interfacial oxidation may provide some insights into this question. However, this can be computationally expensive or possibly formidable in some cases (see the discussion related to Fig. 3). The second question is related to the first one. If the exchange coupling dominates, then the scale should be comparable to the exchange length (typically below 10 nm[60]), otherwise the scale should be comparable to the thickness of the interfacial oxide (FeO$_x$ or CoO$_x$) monolayer (below 0.2 nm)[160]. As a further complication, in a Co/GdO$_x$/AlO$_x$ magneto-electric heterostruture where the Co film is relatively thick (15 nm), a very recent study by Gilbert et al.[29] revealed that the interfacial oxidation mechanism can remain active through the entire Co film, not limited to the interface region.

Role of microstructure in magnetoelectric coupling. In addition to understanding the microscopic origins of magnetoelectric coupling mechanisms, we believe the other most immediate question is to understand the role of microstructure in magnetoelectric coupling. So far both experimental[161] and modeling[93] works have demonstrated that modulating magnetic domain structure can significantly enhance the direct magnetoelectric coupling. With regard to converse magnetoelectric coupling, experiments have shown that a domain-engineered BiFeO$_3$ film can enable an electric field driven 180° net magnetization reversal.[49] In the future, more efforts are required to understand the role of extended defects (dislocations, grain boundaries, domain walls, antiphase boundaries, etc.) in magnetoelectric coupling. There are other important questions, which includes: (i) How to design and obtain novel ferroic domain structures (e.g., polar vortices[162] and magnetic skyrmions)[163] in magnetoelectric heterostructures to achieve new types of magnetoelectric coupling effects? (ii) How to understand and control the dynamics of ferroic domains in magnetoelectric heterostructures upon the application of ultrafast (e.g., electrical, acoustic, optical) stimuli?

Addressing the questions requires closed-loop efforts between theory, multi-scale computational modeling (especially the combination of atomic-scale calculations with microstructure modeling), and experiments that can provide feedback to the theory and modeling. Meanwhile, if the parameter space is too large to accurately predict using computation-based physical or chemical models, and if there are available large experimental data sets with known inputs (materials, geometries, operation conditions, etc., denoted as **x**) and explicitly given output (e.g., the dominant magnetoelectric coupling mechanism in a magnetoelectric heterostructure, denoted as **y**), it is possible to generate a statistically correct predictive model (i.e., a target function that relates **x** to **y**) by understanding the data with machine learning.[164] In this regard, it is possible to computationally generate a statistically correct answer to a question; see more discussions in the next section.

Perspectives on data-driven computational design of magnetoelectric heterostructures

Data-driven computational materials design, different from the previous two paradigms (see Fig. 1), do not necessarily rely on a

np·j

12

Understanding and designing magnetoelectric heterostructures
J-M Hu et al.

computational-based physical or chemical model to understand/predict the relationship between the properties and the atomic structures or microstructure of a materials. Rather, it relies on high-quality databases of atomic structures, microstructures, and properties of materials and employs big-data approach (which in general refer to machine learning, decorrelation, clustering and visualization techniques)[7] to mine these databases for the purpose of creating predictive models and design principles.

Big-data approach (notably machine learning) has been widely utilized in many aspects of our everyday life (e.g., web searches, content-based filtering in online social networks, and recommendations on e-commence and video-streaming websites), and in some scientific disciplines such as biosciences,[165, 166] astronomy,[167] and particle physics,[168] its application to the field of materials science and engineering, however, is still an emergent area. Specifically, although big-data approaches have been utilized to discover predictive models and design principles from the data of atomic structures and corresponding responses generated by quantum computations,[95–103] structural and functional imaging data obtained by scanning probe microscopy,[1, 169–171] X-ray diffraction data,[172, 173] and even data from archived laboratory notebooks,[174] they have been rarely used to understand and harness the data of materials microstructure and properties generated by mesoscale materials modeling. We

believe that the latter will offer opportunities as many as (and possibly larger than) what integrating big-data approaches with quantum computations have brought and will bring.

In this section, as a starting point for building a database, we compile a relatively comprehensive experimental dataset on the coefficients of converse and direct magnetoelectric coupling in different magnetoelectric heterostructures (see Figs 9 and 10 and correspondingly in Tables 3a–3d and Tables 4a–4e). Given the enormous amount of publications in this field, it is likely that some important data might be missing. Nevertheless, this dataset is a good starting point: we will be updating it constantly. Interested readers are encouraged to contact us with new data or/and remind us of the important missing data points. We hope this experimental dataset can provide a basis for the data-driven computational design of magnetoelectric materials. A perspective on this new paradigm will be given following the dataset discussion.

Experimental dataset on the converse and direct magnetoelectric coupling coefficients. Figure 9a shows the magnitudes of both the applied electric field (E) and the resultant magnetization change ($\mu_0 \Delta M = \mu_0(M(E) - M(E = 0))$) extracted from a number of experimental reports that cover the converse magnetoelectric coupling enabled through electrically modulated spin-polarized
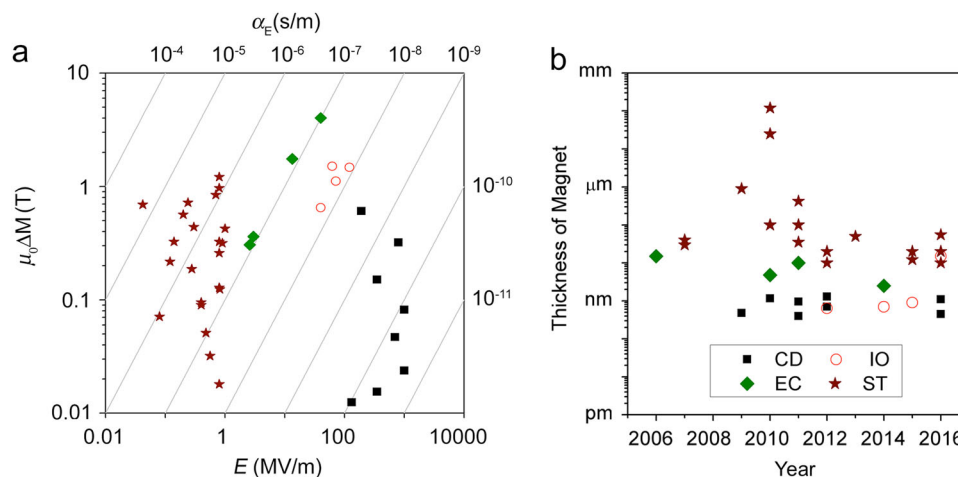

Fig. 9 Some experimental reports of converse magnetoelectric coupling in magnetoelectric heterostructures, sorted by **a** plotting the electrically induced change of magnetization ($\mu_0 \Delta M$) as a function of applied electric field (E), and **b** the thickness of the constituting magnetic layer in a chronological order. The *gray lines* in **a** indicate different levels of $\alpha_E (= \mu_0 \Delta M/E)$. CD Charge Densities, IO Interfacial Oxidation, EC Exchange Coupling, ST Strain Transfer. See Tables 1a–d for details

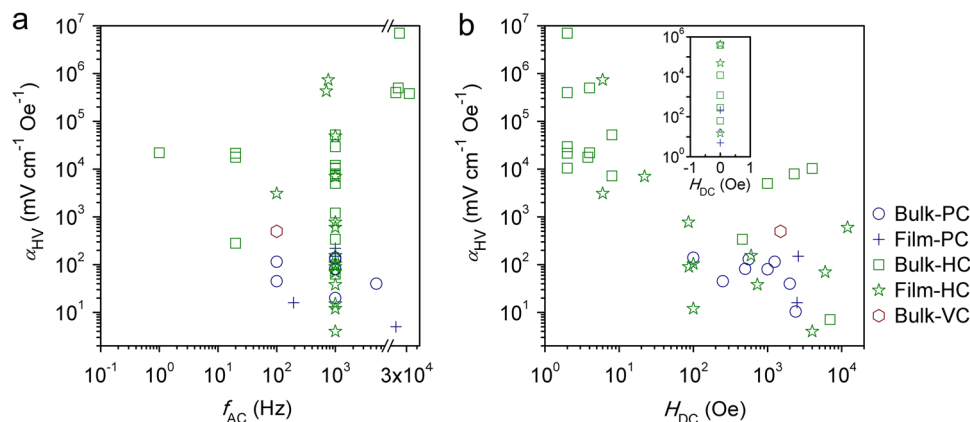**Fig. 10** Some experimental reports of direct magnetoelectric coupling in bulk and thin-film magnetoelectric composites, sorted by plotting the magnetoelctric voltage coefficient $\alpha_{HV}(= \Delta E/\Delta H)$ as a function of **a** the frequency of the driving AC magnetic field (f_{AC}), and **b** the DC bias magnetic field (H_{DC}). PC Particulate Composites, HC Horizontal Composites, VC Vertical Composites

Understanding and designing magnetoelectric heterostructures
J-M Hu et al.

npj

13

Table 3a. Some experimental reports of converse magnetoelectric coupling in horizontal magnetoelectric heterostructures, mediated by electrically driven change of interfacial charge densities

Heterostructure	E (MV/m)	$\mu_0\Delta M$ (Tesla)	α_E (s/m)	Note	Ref.
MgO/Fe (0.48)/Au	132.4	0.012	9.427E-11	MOKE, @Remanence, ΔK_s = 63.4 fJ/(Vm)	[63]
MgO/Co$_{40}$Fe$_{40}$B$_{20}$ (1.16)/Ta	350.0	0.015	4.423E-11	Hall Transport, @Remanence, ΔK_s = 33 fJ/(Vm)	[175]
P(VDF-TrFE)/Co (0.95)/Pt or Pd	800.0	0.320	4.001E-10	MOKE, @Remanence	[176]
HfO$_2$/Co (0.4)/Cr/Au	192.0	0.605	3.153E-09	Hall Transport, @Remanence	[120]
MgO/Co$_{40}$Fe$_{40}$B$_{20}$ (1.3)/Ta	700.0	0.047	6.701E-11	ΔK_s = 50 fJ/(Vm)[a]	[177]
MgO/Fe$_{80}$Co$_{20}$ (0.7)/Au	1000.0	0.052	5.160E-11	ΔK_s = 38.5 fJ/(Vm)[a]	[133]
MgO/Co$_{20}$Fe$_{60}$B$_{20}$ (1.1)/Bottom Electrode	1000.0	0.024	2.372E-11	ΔK_s = 32 fJ/(Vm)[a]	[178]
MgO/Fe (0.45)/Cr	350.0	0.151	4.309E-10	ΔK_s = 290 fJ/(Vm)[b]	[179]

The thickness of the magnetic layer is indicated (in the unit of nanometer)
ΔK_s denotes the magnitude of voltage-controlled magnetic anisotropy; '@Remanece' indicates that we calculated ΔM using the values of remanent magnetization (M_r) in a magnetic hysteresis loop measured with or without E, i.e., $\Delta M = M_r(E) - M_r(E = 0)$
[a] The magnitude of ΔK_s embodies the strength of magnetoelectric coupling. Given that the magnitudes of α_{E-0} and ΔK_{s-0} are both available in a similar heterostructure reported by Endo et al. (ref. [175]), the magnitude of α_E in the present work can be estimated by using the heterostructure as an reference, i.e., $\alpha_E = (\Delta K_s / \Delta K_{s-0}) \times \alpha_{E-0}$
[b] α_E in this work was estimated using a similar procedure described in note a, but using a reference hetorostructure reported by Maruyama et al. (ref. [63])

Table 3b. Converse magnetoelectric coupling mediated by electrically modulated degree of interfacial oxidation, also known as 'magneto-ionic' control of magnetism according to Beach et al.[28]

Heterostructure	E (MV/m)	$\mu_0\Delta M$ (Tesla)	α_E (s/m)	Note	Ref.
ZrO$_2$/MgO/Fe (0.64)/Ag(001)	71.4	1.114	1.560E-08	MOKE, @Remanence, ΔK_s = 944 fJ/(Vm)	[30]
Gd$_2$O$_3$/Co (0.7)/Pt	62.5	1.508	2.413E-08	Hall Transport, @Remanence, ΔK_s = 11600 fJ/(Vm)	[27]
GdO$_x$/Co (0.9)/Pt	121.2	1.477	1.218E-08	MOKE, @Remanence, ΔK_s = 5000 fJ/(Vm), @200°C	[28]
AlO$_x$/GdO$_x$/Co(15)/Pd	39.9	0.65	1.628E-08	VSM, @Remanence, @230°C	[29]

VSM vibrating sample magnetometer

Table 3c. Converse magnetoelectric coupling mediated by the transfer of E-induced strain across the interface

Heterostructure	E (MV/m)	$\mu_0\Delta M$ (Tesla)	α_E (s/m)	Note	Ref.
BTO(001)/La$_{0.67}$Sr$_{0.33}$MnO$_3$(40)	0.4	0.090	2.260E-07	VSM, @H_{bias} = 20 Oe, @ 199 K	[180]
0.72PMN-0.28PT(001)/La$_{0.7}$Sr$_{0.3}$MnO$_3$ (30)	0.6	0.032	5.620E-08	SQUID, @H_{bias} = 100 Oe, @ 330 K	[116]
0.69PMN-0.31PT(011)/Fe$_3$O$_4$(900)	0.8	0.124	1.513E-07	VSM, @Remanence	[181]
BTO(001)/Ni (100)	0.1	0.071	8.880E-07	SQUID, @H_{test} = 0	[182]
0.7PMN-0.3PT (011)/FeCoV(120,000)	0.8	0.128	1.600E-07	VSM, @Remanence	[183]
PIN-PMN-PT (011)/Metglas	0.2	0.026	1.300E-7	VSM@H_{bias} = 50 Oe	[41]
BSPT ceramic/Fe(420)	0.9	0.316	3.510E-07	MOKE, @Remanence	[184]
PZT ceramic/Fe(100)	0.3	0.439	1.464E-06	SQUID, @Remanence	[185]
0.78PMN-0.32PT(011)/Ni(35)	0.1	0.325	2.324E-06	MOKE, @Remanence	[37]
0.7PMN-0.3PT (001)/Co$_{40}$Fe$_{40}$B$_{20}$(20)	0.1	0.217	1.810E-06	SQUID, @H_{test} = 0	[38]
BaTiO$_3$(001)/Co$_{60}$Fe$_{40}$(10)	0.2	0.720	3.000E-06	MOKE,[a] @Remanence	[186]
0.93PZN-0.07PT (011)/FeGaB (50)	0.7	0.844	1.206E-06	VSM, @Remanence	[187]
BTO/Fe(1)/Cu(9)/[Cu(9)/Ni(2)]$_5$	1.0	0.424	4.243E-07	MOKE, @Remanence	[188]
0.78PMN-0.32PT (011)/Ni(20)	0.4	0.095	2.367E-07	SQUID, @Remanence	[189]
0.7PMN-0.3PT(011)/Ta/Pt/Ir$_{25}$Mn$_{75}$/Co$_{40}$Fe$_{40}$B$_{20}$ (55)	0.8	1.213	1.516E-06	SQUID,[b] @H_{test} = 0	[190]
0.67PMN-0.33PT/Co$_{40}$Fe$_{40}$B$_{20}$ (20)	0.2	0.565	2.825E-06	SQUID, @H_{test} = 0	[191]
0.68PMN-0.32PT/Ni(10)	0.3	0.187	6.712E-07	VSM, @H_{test} = 0	Private Communication with M. Ghidini and N.D. Mathur

PIN-PMN-PT Pb(In$_{1/2}$Nb$_{1/2}$)O$_3$–Pb(Mg$_{1/3}$Nb$_{2/3}$)O$_3$–PbTiO$_3$, *BSPT* BiScO$_3$–PbTiO$_3$, *Metglas* FeBSiC
'@H_{test} = 0' indicates that the magnetization data was experimentally recorded in the absence of a testing magnetic field, with $\Delta M = M(E) - M(E = 0)$
[a] Although MOKE detects the local ΔM, the authors (Lahtinen et al.) made a rational assumption to estimate the global α_E (see details in ref. [186])
[b] The sign of magnetization reverses under E

npj

Understanding and designing magnetoelectric heterostructures
J-M Hu et al.

14

Table 3d. Converse magnetoelectric coupling mediated by electrically controlled exchange coupling across the interface

Heterostructure	E (MV/m)	$\mu_0 \Delta M$ (Tesla)	α_E (s/m)	Note	Ref.
YMnO$_3$/Py (15)	13.3	1.751	1.313E-07	SQUID, @H_{bias} ≈100 Oe, @ 2 K, Initial H-field cooling needed	[50]
Cr$_2$O$_3$(0001)/(Co$_{0.6}$Pd$_1$)$_3$ (4.8)/Pd	2.6	0.305	1.175E-07	MOKE, @H_{bias} ≈114 Oe, @ 303 K, Initial magnetelectric field cooling [a] needed	[56]
LuMnO$_3$(0001)/Py (10)/Pt	3.0	0.362	1.205E-07	SQUID, @H_{bias} ≈9.5 Oe, @ 5 K, Initial H-field cooling needed	[51]
BiFeO$_3$/Co$_{0.9}$Fe$_{0.1}$(2.5)/Pt	40.0	4.021	1.005E-07	XMCD-PEEM, purely E-field control [b]	[49]

SQUID superconducting quantum interference device, *PEEM* photoemission electron microscopy, *Py* Permalloy '@H_{bias}' indicates that the magnetization change is experimentally recorded in the presence a static bias magnetic field
[a] Magnetoelectric field cooling: the sample was exposed to both a static magnetic field and a static electric field during cooling
[b] This is so far the only experimental work that demonstrates (via XMCD-PEEM) a purely electric-field-driven 180° switching of net magnetization. We estimated the magnitude of α_E in this work by assuming a 180° magnetization switching in a single-domain magnet, i.e., $\alpha_E = 2\mu_0 M_s/E_c$, where M_s represents the saturation magnetization and E_c denotes the ferroelectric coercive field

Table 4a. Some experimental reports on the magnitude of direct magnetoelectric coupling, α_{HV}, at room temperature in bulk particulate magnetoelectric composites

Heterostructure	H_{DC} (Oe)	f_{AC} (Hz)	α_{HV} (mV cm^{-1} Oe^{-1})	Note	Ref.
0.62BTO-0.38CoFe$_2$O$_4$ (1.5 wt% excess TiO$_2$	560	1000	130	Longitudinal, 3-3 compos.	[193]
0.6BTO-0.4Ni(Co,Mn)Fe$_2$O$_4$	500	1000	81.7	Longitudinal, 3-3 compos.	[194]
Ni$_{0.8}$Zn$_{0.2}$Fe$_2$O$_4$-0.41 vol% PZT	250	100	45	Transverse, 3-0 compos.	[195]
PZT-20 wt%NiCo$_{0.02}$Cu$_{0.02}$Mn$_{0.1}$Fe$_{1.8}$O$_4$	1250	100	115	Longitudinal, 3-0 compos.	[196]
PMN-PT-NiFe$_2$O$_4$	2400	0	10.43	Transverse, 3-0 compos.	[197]
0.68Pb(Zr$_{0.57}$Ti$_{0.43}$)O$_3$-0.32NiFe$_2$O$_4$	1000	1000	80	Longitudinal, 3-0 compos.	[198]
0.9Pb(Zr$_{0.52}$Ti$_{0.48}$)O$_3$-0.1NiFe$_{1.9}$Mn$_{0.1}$O$_4$	100	1000	140	Longitudinal, 3-0 compos.	[199]
P(VDF-TrFE)-CoFe$_2$O$_4$	2000	5000	40	Longitudinal, 3-0 compos.	[200]

'Longitudinal' and 'transverse' indicate that the testing magnetic fields (including both the bias H_{DC} and the driving H_{AC}) are applied parallel and perpendicular to the orientation of electric polarization, respectively. '3-3' type connectivity of composites suggests a random mixture of grains of the two constituent phases; '3-0' type connectivity indicate a (e.g., piezoelectric) matrix ('3') with embedded (e.g., magnetostrictive) particles.

Table 4b. Room-temperature α_{HV} in thin-film particulate magnetoelectric composites (compos.)

Heterostructure	H_{DC} (Oe)	f_{AC} (Hz)	α_{HV} (mV cm^{-1} Oe^{-1})	Note	Ref.
PbZr$_{(0.52}$Ti$_{0.48)}$O$_3$-CoFe$_2$O$_4$	0	1000	220	3-0 compos., sol-gel	[201]
0.65Pb(Zr$_{0.52}$Ti$_{0.48}$)O$_3$-0.35NiFe$_2$O$_4$	2500	194	16	Longitudinal, 3-0 compos., PLD	[202]
NCZF/0.8PZT-0.2PZN	2600	1000	150	Transverse, 3-0 compos., AD	[203]
BiFeO$_3$-CoFe$_2$O$_4$	2900	N/A[a]	338	Transverse, 3-0 compos., PLD	[204]

NCZF (Ni$_{0.6}$Cu$_{0.2}$Zn$_{0.2}$)Fe$_2$O$_4$, *PZN* Pb(Zn$_{1/3}$Nb$_{2/3}$)O$_3$, *PLD* pulsed laser deposition, *AD* aerosol deposition
[a] The α_{HV} was obtained indirectly by measuring the piezoresponse displacement loop (using piezoresponse force microscopy) with or without applying an in-plane DC magnetic field, and therefore represents the local magnetoelectric response rather than a global one from macroscopic measurements

charge densities,[63, 120, 133, 175–179] degree of interfacial oxidation,[27–30] exchange coupling,[49–51, 56] or/and transfer of electric-field-induced strains.[37, 38, 41, 116, 180–192] We term these four types of converse magnetoelectric coupling mechanisms as 'charge densities', 'interfacial oxidation', 'exchange coupling', and 'strain transfer', respectively. Note that the change of magnetization (ΔM) can be global (that is, average of an entire heterostructure), which can be measured directly using, for example, a superconducting quantum interference device or indirectly from the Hall transport measurement; the ΔM can also represent the magnetization change within a local surface area (precisely, including surface regions within the probe depth) of the sample, which can be measured through various magnetic domain imaging techniques (see a summary in ref. 12). Details of the characterization techniques and conditions for the data points in Fig. 9a can be found in Tables 3a–d. Figure 9b displays the thickness of the

magnet corresponding to the experimental reports in Fig. 9a.

The upper left region of Fig. 9a suggests heterostructures with relatively strong magnetoelectric coupling. This region is occupied by magnetoelectric heterostructures that exhibit the 'strain transfer' mechanism, including so far the largest magnetoelectric coupling coefficient of about 1.6×10^{-5} s/m reported in a FeRh/BaTiO$_3$ heterostructure. This gigantic magnetoelectric coupling has been achieved at 385 K (above room temperature) mainly through strain-mediated electric-field-driven ferromagnetic to AF phase transition in FeRh.[192] The data points in Fig. 9a reveal that the converse magnetoelectric coupling enabled through 'exchange coupling' > 'interfacial oxidation' > 'charge densities', and that in general the converse magnetoelectric coupling enabled through 'strain transfer' > 'exchange coupling' except three data points. For practical magnetoelectric device applications, other attributes such as energy consumption (goal: down to

Understanding and designing magnetoelectric heterostructures
J-M Hu et al.

npj

15

Table 4c. Room-temperature α_{HV} in bulk horizontal magnetoelectric composites

Heterostructure	H_{DC} (Oe)	f_{AC} (Hz)	α_{HV} (mV cm^{-1} Oe^{-1})	Note	Ref.
Terfenol-D/PMN-PT/Terfenol-D	4000	1000	10300	Longitudinal, 2/2 compos.	[206]
Metglas/PVDF/Metglas	8	1000	7200	Transverse, 2/2 compos.	[207]
Ni/Doped-BaTiO$_3$[a]	7000	0	7.1	Longitudinal, 2/2 compos.	[208]
PZT/Ni$_{0.7}$Zn$_{0.3}$Fe$_2$O$_4$/Ni	0	20	280	Transverse, 2/2 compos.	[209]
Metglas/PMT	0	1000	63.3	Transverse, 2/2 compos.	[210]
NCZF/textured 0.675PMN-0.325PT/NCZF	0	1000	1200	Transverse, 2/2 compos.	[211]
Terfenol-D/PVDF/Terfenol-D	2300	1000	7930	Longitudinal, 2/2 compos., Shear mode	[212]
Metglas/PVDF	2	20	21460	Transverse,[b] 2/2 compos.	[213]
FeBSiC/PZT (fiber)/FeBSiC	4	1 (22000)	22000 (500000)	Longitudinal, 2/1 compos.[c]	[214]
FeBSiC/PZN-PT (fiber)/FeBSiC	2	1000 (20000)	10500 (400000)	Transverse, 2/1 compos.[b]	[215]
Metglas/PMN-PT (fiber)/Metglas	8	1000	52000	Longitudinal, 2/1 compos.[c]	[216]
Metglas/PZT (fiber)/Metglas	0	1000 (33700)	12000 (380000)	Longitudinal, 2/1 compos.[c]	[217]
Metglas (fiber)/PMN-PT (fiber)/Metglas (fiber)	2	1000 (23000)	29310 (7000000)	Transverse, 1/1 compos.[b]	[229]

[a] A commercial multilayer capacitors consisting of Ni electrodes and BaTiO$_3$-based dielectric layers. The DC magnetic field is applied parallel to electric polarization in BaTiO$_3$ through VSM
[b] Enhanced magnetic flux concentration inside the Metglas (FeBSiC) ribbon can enhance the magnitude of α_{HV}
[c] The '2 - 1' type phase connectivity leads to a significantly enhanced α_H by magnifying the induced voltage
PMT: 0.8[Pb(Zr$_{0.52}$Ti$_{0.48}$)O$_3$]-0.2[Pb(Zn$_{1/3}$Nb$_{2/3}$)O$_3$]-2 mol% MnO$_2$

Table 4d. Room-temperature α_{HV} in thin-film horizontal magnetoelectric composites

Heterostructure	H_{DC} (Oe)	f_{AC} (Hz)	α_{HV} (mV cm^{-1} Oe^{-1})	Note	Ref.
NiFe$_2$O$_4$/BTO	100	1000	12	Longitudinal, All-film, PLD	[218]
CoFe$_2$O$_4$/BTO	100	1000	104	Longitudinal, All-film, PLD	[219]
CoFe$_2$O$_4$/PZT	6000	1000	70	Longitudinal, All-film, sol–gel	[220]
Ni$_{0.8}$Zn$_{0.2}$Fe$_2$O$_4$/Pb(Zr$_{0.6}$Ti$_{0.4}$)O$_3$	0	1000	15	Longitudinal, All-film, PLD	[221]
La$_{0.7}$Sr$_{0.3}$MnO$_3$/Pb(Zr$_{0.52}$Ti$_{0.48}$)O$_3$	4000	1000	4	Longitudinal, All-film, PLD	[222]
FeCoSiB/AlN	6	100 (753)	3100 (737000)	Transverse, All-film, Sputtering	[223]
Ir$_{0.3}$Mn$_{0.7}$/FeCoSiB/AlN	0	700	430000	Transverse, All-film, Sputtering	[161]
[BaTiO$_3$–BiFeO$_3$] × 15	0	1000	49000	Longitudinal, SLs, PLD	[228]
BTO/CoFe$_2$O$_4$ (bulk ceramic)	730	1000	38	Transverse, FoS, PLD	[224]
Pb(Zr$_{0.52}$Ti$_{0.48}$)O$_3$/CoFe$_2$O$_4$ (bulk ceramic)	600	1000	155	Transverse, FoS, sol–gel	[225]
BTO/Ni (bulk foil)	87	1000	90	Transverse, FoS, CSD	[226]
Pb(Zr$_{0.52}$Ti$_{0.48}$)O$_3$/Ni (bulk foil)	86	1000	772	Transverse, FoS, sol–gel	[227]
Pb(Zr,Ti)O$_3$/Metglas (bulk foil)	22	1000	7000	Transverse, FoS, GSV deposition with laser annealing	[205]

FeCoSiB (Fe$_{90}$Co$_{10}$)$_{78}$Si$_{12}$B$_{10}$, *FoS* film-on-substrate, *SLs* Superlattices, *CSD* chemical solution deposition, *GSV* granule spray in vacuum

Table 4e. Room-temperature α_{HV} in bulk and thin-film vertical magnetoelectric composites

Heterostructure	H_{DC} (Oe)	f_{AC} (Hz)	α_{HV} (mV cm^{-1} Oe^{-1})	Note	Ref.
PZT-TDE	1500	100	500	Longitudinal, Casting, 1-3 Compos.	[230]
CoFe$_2$O$_4$(core)-PZT(shell) nanofiber	2000	N/A[a]	29,500	Transverse, Electrospinning, Core-shell nanofiber	[231]

TDE Terfenol-D/Epoxy medium
[a] The α_{HV} was obtained indirectly by measuring the piezoresponse displacement loop (using piezoresponse force microscopy) with or without applying an in-plane DC magnetic field, and therefore represents the local magnetoelectric response rather than a global one from macroscopic measurements

the level of attoJoule per unit per driving voltage), operation speed (goal: from GHz to THz), reliability (>10-year service life), and compatibility of the constituent materials with existing technological platforms would also need to be considered.

Figure 10 summarizes experimental reports on the magnitude of room-temperature magnetoelectric voltage coefficient ($\alpha_{HV} = \Delta E/\Delta H$, in the unit of mV cm^{-1} Oe^{-1}) in particulate composites,[193–204] horizontal heterostructures,[161, 205–229] and vertical heterostructures[230, 231] (see details in Tables 4a–e). The α_{HV} is usually measured by detecting the output voltage induced by an externally applied DC bias magnetic field (H_{DC}) and a co-axial AC driving magnetic field (with a frequency f_{AC}).[232] Applying these

npj
Understanding and designing magnetoelectric heterostructures
J-M Hu et al.

16

magnetic fields parallel or perpendicular to the electric polarization is known as measuring α_{HV} in longitudinal or transverse modes, respectively. A transverse α_{HV} of about 7000 V cm^{-1} Oe^{-1} has been observed under $H_{DC} = 2$ Oe and $f_{AC} = 23$ kHz in a 1-1 connectivity horizontal composite consisting of a (011)-oriented Pb(Mg,Nb)O$_3$–PbTiO$_3$ fiber laminated with Metglas (FeBSiC) fiber.[229] This is so far the largest reported value of α_{HV}. With an application to low-cost magnetic field sensors,[19] magnetoelectric heterostructures that exhibit a high α_{HV} under a low f_{AC} (see the top left corner of Fig. 10a) will enable high detection sensitivity to weak and low-frequency magnetic fields. Such ability allows us to potentially utilize magnetoelectrics-based magnetic field sensors for biomedical diagnosis, because magnetic fields generated from the electrical activity of human organs are typically weak (10 fT—1 pT,[233, 234]), and exhibit low frequency (10^{-2}—10^3 Hz[14]). Moreover, high α_{HV} under low or zero H_{DC} is also beneficial to enhancing the detection sensitivity, because a low H_{DC} will significantly reduce the cross-talk among neighboring sensor elements[15] and thereby reduce the noise level. As shown in Fig. 10b, most of the current experiments utilize a relatively low magnetic field (below 1 kOe). Notably, a large α_{HV} of about 430 V cm^{-1} Oe^{-1} (see the inset of Fig. 10b) has been observed under $H_{DC} = 0$ Oe and $f_{AC} = 700$ Hz in an exchange-biased FeCoSiB/AlN all-film horizontal heterostructure.[161] Finally, we note that the most immediate challenge of applying magnetoelectic heterostructures to biomedical diagnosis is to enhance the α_{HV} at $0 < f_{AC} < 1$ Hz, for which there have been no existing experimental reports (see Fig. 10a).
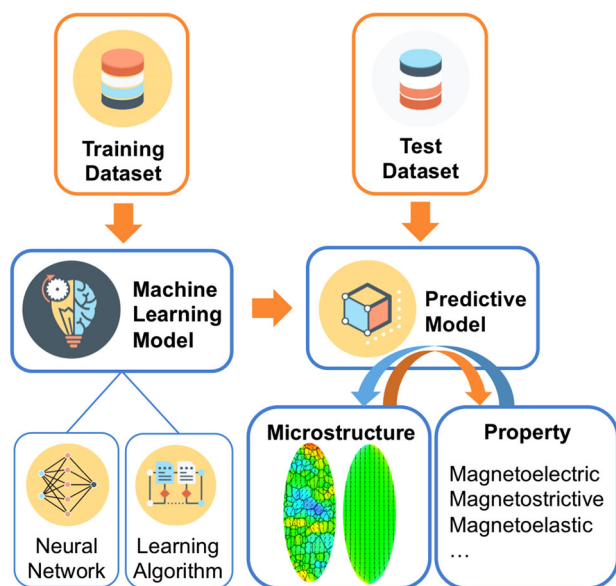

Fig. 11 Envisioned scheme of data-driven computational materials design at the scale of microstructure enabled by supervised machine learning. Training and testing datasets consist of structural and functional imaging data for each spatial location. These data can be obtained through scanning and electron microscopies, where deep-learning imaging recognition can be used to rapidly acquire imaging data and register the structural and functional imaging data. These data can also be obtained through a physical or chemical model. The machine learning model, typically consisting of a neural network and a learning algorithm, aims to discover a statistically correct predictive model from the training datasets. Once passing the test with test dataset, the predictive model can be utilized to predict the materials properties of a newly generated microstructure (see *orange arrow*), and inversely, identify a microstructure that produces optimum properties (see *blue arrow*). Phase-field method is one of the best-suited computational tools to generate these microstructures (e.g., the domain and grain structure in an polycrystalline nanomagnet) for all types of solid-state materials ranging from metals to ceramics and to soft materials

Data-driven computational materials design incorporating materials microstructures. In this section, we will briefly discuss three essentials for a data-driven design of materials microstructure for optimum materials properties, including training and test datasets of microstructure (inputs) and corresponding properties (outputs), microstructure data generation, and machine learning models. As shown in Fig. 11, we propose to utilize a machine learning model (e.g., a feedforward neural network plus backpropagation[235]) to discover a predictive model from the training datasets of microstructure and corresponding properties. The test dataset will be utilized to measure the performance of the predictive model on new microstructures that have never appeared during training. The predictive model is not built on any fundamental principles of physical or chemical processes, yet it is statistically correct and can be utilized to automatically evaluate the properties of newly generated microstructures until the microstructure yielding optimum properties is identified. Note that the machine learning model described above represents a typical example of supervised learning,[164] because the inputs and outputs are explicitly defined and because the machine learning model is trained solely based on the inputs. This is different from an unsupervised learning, which aims to cluster datasets that have no predefined inputs and outputs and build learning models from all clustered datasets such that a casual relation may be discovered in higher levels of abstraction. Unsupervised learning typically exhibits lower statistical accuracy than supervised learning in making predictions especially when there exist multiple ways of clustering datasets, however, it often suits better for understanding datasets with complex causal relations.[236]

High-quality (e.g., low uncertainty and free of outlier features) *training and test datasets* of microstructure (inputs) and properties (outputs) are the foundations for building a predictive model of high statistical accuracy. These data can be obtained experimentally through structural and functional imaging based on scanning and electron microscopies.[7, 169–171] For example, a conductive atomic force microscope has been utilized to map both the topography and corresponding local conductivity of a Co$_2$Fe$_2$O$_4$–BiFeO$_3$ thin-film vertical magnetoeletric composite.[170] Notably, employing the big-data approach to understand and harness high-resolution structural and functional imaging data allows us to register the two, such that structural and functional data for each spatial location can be obtained (see a detailed discussion in ref. 1). In addition, a mesoscale computation-based physical or chemical model can be utilized to clean the imaging data by reducing noise and eliminating outliers (if any). For instance, one can reconstruct 3D electron backscatter diffraction data of grain orientations using data processing tools such as DREAM.3D,[237] and then convert the format of the reconstructed data in such a way that the data can be inputted into a phase-field model of 3D grain growth.[238] After evolving the inputted 3D grain structure for a few time steps, the noisy regions could become clearer and outliers should quickly disappear. Furthermore, a mesoscale computation-based physical or chemical model, once validated and refined based on feedback from experiments, can be directly used to generate the desirable datasets of materials microstructures and properties. Note that a publically available online database of materials microstructures and corresponding properties is still lacking.[6]

Microstructure datasets that have never appeared in training and test datasets will be the input of a tested predictive model (see Fig. 11). Microstructure data can have many tags due to the great complexity of microstructure. For example, describing the microstructure of a magnetic/ferroelectric heterostructure in 3D needs multiple variables, which may include the morphological distributions of (i) two constituent phases η_i ($i = 1,2$), (ii) local magnetization M_j ($j = 1,2,3$) (magnetic domains), (iii) local polarization P_k ($k = 1,2,3$) (ferroelectric domains), and (iv) grain orientations θ_{lm} ($l = 1,2$, $m = 1,2,3...n$) (grain structure, the subscript 'l' is an

Understanding and designing magnetoelectric heterostructures
J-M Hu et al.

npj

17

indicator for the ferroelectric or magnetic phase, while subscript '*m*' indicates the number of different crystallographic orientations) or texture. Therefore it may at least require the use of a total of 13 (=3 + 2 + 3 + 3 + 2) tags to describe all microstructural features in one dataset. And all these microstructural features can contribute to the magnetoelectric coupling.

These input microstructural data can be generated by computational methods. For example, one can generate polycrystal structures via voronoi tessellations, morphological distributions of two-phase composites using random packing,[239] and all types of above-mentioned microstructures using phase-field method.[240] We believe using phase-field method to generate microstructure data is particularly advantageous mainly because of the following two reasons. First, as long as a phase-field model captures the essential thermodynamic and kinetic principles of microstructure formation, microstructures generated by the model would be highly realistic (that is, be able to fabricate and observe experimentally). Second, the model can incorporate the physical interactions among different microstructural variables and may thereby lead to a more accurate prediction of the materials microstructure. For example, our micromagnetic phase-field model can predict the magnetic domain structure in a polycrystalline magnetic dot by integrating conventional micromagnetics with polycrystal anisotropy. Shown on the *bottom right* of Fig. 11 are the magnetic domain structures in a polycrystalline and a single-crystal magnet, both of which have a dimension of 850 nm (full length of in-plane short axis) × 2200 nm (full length of in-plane long axis) × 5 nm (thickness) and a cubic magnetocrystalline anisotropy ($K_1 = 0.02$ MJ/m^3, $K_2 = 0$, where K_1 and K_2 are the bulk anisotropy coefficients). As shown, different local crystallographic orientations in different grains can deter the local magnetization vector from aligning along the in-plane long axis.

Machine learning model has rarely been utilized to understand and harness the data of microstructures and corresponding properties as mentioned above, and has not been applied to design microstructures for optimum magnetoelectric coupling. However, several relevant attempts have been made. For example, Liu et al.[241] developed a machine learning model that can identify the suitable polygrain structures that would lead to a strong magnetostrictive coupling, which is relevant to a strain-mediated magnetoelectric coupling. In future works, magnetic domain structures, which govern the magnetostrictive coupling, should also be included in the space of design variables. More recently, Ward et al.[101] proposed a general-purpose machine learning model that enables predicting properties of inorganic materials using the training and test databases of atomic structures and corresponding properties established from DFT calculations.[242] This machine learning model may be adapted to understand the data of microstructures and corresponding properties. In particular, established microstructure-property correlation may improve the efficiency and reliability of a machine learning model. For example, it is known that ferroelectric or ferromagnetic materials with multiple coexisting phases of similar energy level may show superior piezoelectric[243] or magnetostrictive[244] properties. Both properties are important to achieving a strong strain-mediated magnetoelectric coupling. With this knowledge, we may organize the data of microstructures with coexisting multiple phases and their corresponding properties in one group, and train a predictive model separately for this group. Such confluence of our knowledge of the physical and chemistry of a material system and big-data approaches has been termed as a 'deep-data' approach.[1]

Overall, the proposed data-driven computational approach of designing materials microstructure will be particularly useful when the number of design variables is too large to allow us to develop or employ a mesoscale physical or chemical model, or/and when running a physical or chemical model is computationally too expensive or formidable. However, this is a very daunting task with very few relevant existing reports. Indeed, there is still plenty

of space for future work on the data-driven computational materials design at the scale of microstructure,[245] which bridges the well-established macroscopic structure design with the rapidly developing atomic-scale materials design.

AUTHOR CONTRIBUTIONS

J.M.H. and L.Q.C. designed the outline of this article. J.M.H. compiled the experimental datasets. J.M.H. wrote the paper based on detailed edits and suggestions from L.Q.C., and based on substantial feedback from C.G.D. and C.W.N.

COMPETING INTERESTS

The authors declare that they have no competing financial interests.

REFERENCES

1. Kalinin, S. V., Sumpter, B. G. & Archibald, R. K. Big-deep-smart data in imaging for guiding materials design. *Nat. Mater.* **14**, 973–980 (2015).
2. Kalidindi, S. R. & Graef, M. D. Materials data science: current status and future outlook. *Annu. Rev. Mater. Res.* **45**, 171–193 (2015).
3. Rajan, K. Materials Informatics: The Materials "Gene" and Big Data. *Annu. Rev. Mater. Res.* **45**, 153–169 (2015).
4. Agrawal, A. & Choudhary, A. Perspective: materials informatics and big data: realization of the "fourth paradigm" of science in materials science. *APL Mater.* **4**, 053208 (2016).
5. Lookman, T., Alexander, F. J. & Bishop, A. R. Perspective: codesign for materials science: an optimal learning approach. *APL Mater.* **4**, 053501 (2016).
6. Hill, J. et al. Materials science with large-scale data and informatics: unlocking new opportunities. *MRS. Bull.* **41**, 399–409 (2016).
7. Sumpter, B. G., Vasudevan, R. K., Potok, T. & Kalinin, S. V. A bridge for accelerating materials by design. *npj Comput. Mater.* **1**, 15008 (2015).
8. Kalil, T. & Wadia, C. Materials genome initiative for global competitiveness (2011). Available at http://www.whitehouse.gov/sites/default/files/microsites/ostp/materials_genome_initiative-final.pdf.
9. Dong, S., Liu, J.-M., Cheong, S.-W. & Ren, Z. Multiferroic materials and magnetoelectric physics: symmetry, entanglement, excitation, and topology. *Adv. Phys.* **64**, 519–626 (2015).
10. Matsukura, F., Tokura, Y. & Ohno, H. Control of magnetism by electric fields. *Nat. Nanotechnol.* **10**, 209–220 (2015).
11. Ortega, N., Ashok, K., Scott, J. F. & Ram, S. K. Multifunctional magnetoelectric materials for device applications. *J. Phys. Condens. Matter.* **27**, 504002 (2015).
12. Hu, J.-M., Chen, L.-Q. & Nan, C.-W. Multiferroic heterostructures integrating ferroelectric and magnetic materials. *Adv. Mater.* **28**, 15–39 (2016).
13. Song, C., Cui, B., Li, F., Zhou, X. & Pan, F. Recent progress in voltage control of magnetism: materials, mechanisms, and performance. *Prog. Mater. Sci.* **87**, 33–82 (2017).
14. Zhai, J., Xing, Z., Dong, S., Li, J. & Viehland, D. Detection of pico-Tesla magnetic fields using magneto-electric sensors at room temperature. *Appl. Phys. Lett.* **88**, 062510 (2006).
15. Lage, E. et al. Exchange biasing of magnetoelectric composites. *Nat. Mater.* **11**, 523–529 (2012).
16. Fusil, S., Garcia, V., Barthélémy, A. & Bibes, M. Magnetoelectric devices for spintronics. *Annu. Rev. Mater. Res.* **44**, 91–116 (2014).
17. Nikonov, D. E. & Young, I. A. Benchmarking spintronic logic devices based on magnetoelectric oxides. *J. Mater. Res.* **29**, 2109–2115 (2014).
18. Wang, Y., Li, J. & Viehland, D. Magnetoelectrics for magnetic sensor applications: status, challenges and perspectives. *Mater. Today* **17**, 269–275 (2014).
19. Hu, J.-M., Nan, T., Sun, N. X. & Chen, L.-Q. Multiferroic magnetoelectric nanostructures for novel device applications. *MRS. Bull.* **40**, 728–735 (2015).
20. Fiebig, M., Lottermoser, T., Meier, D. & Trassin, M. The evolution of multiferroics. *Nat. Rev. Mater.* **1**, 16046 (2016).

npj

Understanding and designing magnetoelectric heterostructures
J-M Hu et al.

18

21. Rondinelli, J. M., Stengel, M. & Spaldin, N. A. Carrier-mediated magnetoelectricity in complex oxide heterostructures. *Nat. Nanotechnol.* **3**, 46–50 (2008).

22. Duan, C.-G. et al. Surface magnetoelectric effect in ferromagnetic metal films. *Phys. Rev. Lett.* **101**, 137201 (2008).

23. Maier, J. *Physical Chemistry of Ionic Materials: Ions and Electrons in Solids.* (Wiley, 2004).

24. Cai, T. et al. Magnetoelectric coupling and electric control of magnetization in ferromagnet/ferroelectric/normal-metal superlattices. *Phys. Rev. B* **80**, 140415 (2009).

25. Zhang, S. Spin-dependent surface screening in ferromagnets and magnetic tunnel junctions. *Phys. Rev. Lett.* **83**, 640–643 (1999).

26. Bauer, U., Emori, S. & Beach, G. S. D. Voltage-controlled domain wall traps in ferromagnetic nanowires. *Nat. Nanotechnol.* **8**, 411–416 (2013).

27. Bi, C. et al. Reversible control of co magnetism by voltage-induced oxidation. *Phys. Rev. Lett.* **113**, 267202 (2014).

28. Bauer, U. et al. Magneto-ionic control of interfacial magnetism. *Nat. Mater.* **14**, 174–181 (2015).

29. Gilbert, D. A. et al. Structural and magnetic depth profiles of magneto-ionic heterostructures beyond the interface limit. *Nat. Commun.* **7**, 12264 (2016).

30. Bauer, U., Przybylski, M., Kirschner, J. & Beach, G. S. D. Magnetoelectric charge trap memory. *Nano. Lett.* **12**, 1437–1442 (2012).

31. Rajanikanth, A., Hauet, T., Montaigne, F., Mangin, S. & Andrieu, S. Magnetic anisotropy modified by electric field in V/Fe/MgO(001)/Fe epitaxial magnetic tunnel junction. *Appl. Phys. Lett.* **103**, 062402 (2013).

32. Bonell, F. et al. Reversible change in the oxidation state and magnetic circular dichroism of Fe driven by an electric field at the FeCo/MgO interface. *Appl. Phys. Lett.* **102**, 152401 (2013).

33. Manchon, A. et al. X-ray analysis of the magnetic influence of oxygen in Pt/Co/AlO$_x$ trilayers. *J. Appl. Phys.* **103**, 07A912 (2008).

34. Manchon, A. et al. Analysis of oxygen induced anisotropy crossover in Pt/Co/MO$_x$ trilayers. *J. Appl. Phys.* **104**, 043914 (2008).

35. Hu, J.-M. & Nan, C. W. Electric-field-induced magnetic easy-axis reorientation in ferromagnetic/ferroelectric layered heterostructures. *Phys. Rev. B* **80**, 224416 (2009).

36. Hu, J.-M., Nan, C.-W. & Chen, L.-Q. Size-dependent electric voltage controlled magnetic anisotropy in multiferroic heterostructures: interface-charge and strain comediated magnetoelectric coupling. *Phys. Rev. B* **83**, 134408 (2011).

37. Wu, T. et al. Giant electric-field-induced reversible and permanent magnetization reorientation on magnetoelectric Ni/(011) [Pb(Mg$_{1/3}$Nb$_{2/3}$)O$_3$]$_{(1-x)}$-[PbTiO$_3$]$_x$ heterostructure. *Appl. Phys. Lett.* **98**, 012504 (2011).

38. Zhang, S. et al. Electric-field control of nonvolatile magnetization in Co$_{40}$Fe$_{40}$B$_{20}$/Pb(Mg$_{1/3}$Nb$_{2/3}$)$_{0.7}$Ti$_{0.3}$O$_3$ structure at room temperature. *Phys. Rev. Lett.* **108**, 137203 (2012).

39. Lu, Y. et al. Phase transitional behavior and piezoelectric properties of the orthorhombic phase of Pb(Mg$_{1/3}$Nb$_{2/3}$)O$_3$–PbTiO$_3$ single crystals. *Appl. Phys. Lett.* **78**, 3109–3111 (2001).

40. Wang, Z., Wang, Y., Ge, W., Li, J. & Viehland, D. Volatile and nonvolatile magnetic easy-axis rotation in epitaxial ferromagnetic thin films on ferroelectric single crystal substrates. *Appl. Phys. Lett.* **103**, 132909 (2013).

41. Staruch, M., Li, J. F., Wang, Y., Viehland, D. & Finkel, P. Giant magnetoelectric effect in nonlinear Metglas/PIN-PMN-PT multiferroic heterostructure. *Appl. Phys. Lett.* **105**, 152902 (2014).

42. Liu, M. et al. Electrically controlled non-volatile switching of magnetism in multiferroic heterostructures via engineered ferroelastic domain states. *NPG Asia Mater.* **8**, e316 (2016).

43. Zhang, J. et al. A nanoscale shape memory oxide. *Nat. Commun.* **4**, 2768 (2013).

44. Hu, J.-M., Yang, T. N., Chen, L. Q. & Nan, C. W. Voltage-driven perpendicular magnetic domain switching in multiferroic nanoislands. *J. Appl. Phys.* **113**, 194301 (2013).

45. Yang, T. N., Hu, J.-M., Nan, C. W. & Chen, L. Q. On the elastically coupled magnetic and ferroelectric domains: a phase-field model. *Appl. Phys. Lett.* **104**, 202402 (2014).

46. Liu, M. & Sun, N. X. Voltage control of magnetism in multiferroic heterostructures. *Phil. Trans R. Soc. A* **372**, 20120439 (2014).

47. Zhao, T. et al. Electrical control of antiferromagnetic domains in multiferroic BiFeO$_3$ films at room temperature. *Nat. Mater.* **5**, 823–829 (2006).

48. Lebeugle, D. et al. Electric-field-induced spin flop in BiFeO$_3$ single crystals at room temperature. *Phys. Rev. Lett.* **100**, 227602 (2008).

49. Heron, J. T. et al. Deterministic switching of ferromagnetism at room temperature using an electric field. *Nature* **516**, 370–373 (2014).

50. Laukhin, V. et al. Electric-field control of exchange bias in multiferroic epitaxial heterostructures. *Phys. Rev. Lett.* **97**, 227201 (2006).

51. Skumryev, V. et al. Magnetization reversal by electric-field decoupling of magnetic and ferroelectric domain walls in multiferroic-based heterostructures. *Phys. Rev. Lett.* **106**, 057206 (2011).

52. Ederer, C. & Spaldin, N. A. Weak ferromagnetism and magnetoelectric coupling in bismuth ferrite. *Phys. Rev. B* **71**, 060401 (2005).

53. Mathur, N. Materials science: a desirable wind up. *Nature* **454**, 591–592 (2008).

54. Goltsev, A. V., Pisarev, R. V., Lottermoser, T. & Fiebig, M. Structure and interaction of antiferromagnetic domain walls in hexagonal YMnO$_3$. *Phys. Rev. Lett.* **90**, 177204 (2003).

55. Eiichi, H., Katsumi, H. & Yukito, T. Clamping of ferroelectric and antiferromagnetic order parameters of YMnO$_3$. *J. Phys. Condens. Matter.* **15**, L103–L109 (2003).

56. He, X. et al. Robust isothermal electric control of exchange bias at room temperature. *Nat. Mater.* **9**, 579–585 (2010).

57. Wu, N. et al. Imaging and control of surface magnetization domains in a magnetoelectric antiferromagnet. *Phys. Rev. Lett.* **106**, 087202 (2011).

58. Trassin, M. et al. Interfacial coupling in multiferroic/ferromagnet heterostructures. *Phys. Rev. B* **87**, 134426 (2013).

59. Zhou, Z. et al. Probing electric field control of magnetism using ferromagnetic resonance. *Nat. Commun.* **6**, 6082 (2015).

60. Abo, G. S. et al. Definition of magnetic exchange length. *IEEE. Trans. Magn.* **49**, 4937–4939 (2013).

61. Ohno, H. et al. Electric-field control of ferromagnetism. *Nature* **408**, 944–946 (2000).

62. Weisheit, M. et al. Electric field-induced modification of magnetism in thin-film ferromagnets. *Science* **315**, 349–351 (2007).

63. Maruyama, T. et al. Large voltage-induced magnetic anisotropy change in a few atomic layers of iron. *Nat. Nanotechnol.* **4**, 158–161 (2009).

64. Niranjan, M. K., Velev, J. P., Duan, C.-G., Jaswal, S. S. & Tsymbal, E. Y. Magnetoelectric effect at the Fe$_3$O$_4$/BaTiO$_3$ (001) interface: a first-principles study. *Phys. Rev. B* **78**, 104405 (2008).

65. Niranjan, M. K., Duan, C.-G., Jaswal, S. S. & Tsymbal, E. Y. Electric field effect on magnetization at the Fe/MgO(001) interface. *Appl. Phys. Lett.* **96**, 222504 (2010).

66. Nakamura, K., Akiyama, T., Ito, T., Weinert, M. & Freeman, A. J. Role of an interfacial FeO layer in the electric-field-driven switching of magnetocrystalline anisotropy at the Fe/MgO interface. *Phys. Rev. B* **81**, 220409 (2010).

67. Yoichi, S. et al. Voltage-assisted magnetization switching in Ultrathin Fe$_{80}$Co$_{20}$ alloy layers. *Appl. Phys. Express* **2**, 063001 (2009).

68. Song, O., Ballentine, C. A. & O'Handley, R. C. Giant surface magnetostriction in polycrystalline Ni and NiFe films. *Appl. Phys. Lett.* **64**, 2593–2595 (1994).

69. Heron, J. T. et al. Electric-field-induced magnetization reversal in a ferromagnet-multiferroic heterostructure. *Phys. Rev. Lett.* **107**, 217202 (2011).

70. Mathur, N. Materials science: a desirable wind up. *Nature* **454**, 591–592 (2008).

71. Wang, J. J. et al. Effect of strain on voltage-controlled magnetism in BiFeO$_3$-based heterostructures. *Sci. Rep.* **4**, 4553 (2014).

72. Dzyaloshinsky, I. A thermodynamic theory of "weak" ferromagnetism of antiferromagnetics. *J. Phys. Chem. Solids.* **4**, 241–255 (1958).

73. Moriya, T. Anisotropic superexchange interaction and weak ferromagnetism. *Phys. Rev.* **120**, 91–98 (1960).

74. Sando, D. et al. Crafting the magnonic and spintronic response of BiFeO$_3$ films by epitaxial strain. *Nat. Mater.* **12**, 641–646 (2013).

75. Svanberg, K. The method of moving asymptotes—a new method for structural optimization. *Int. J. Numer. Meth. Eng.* **24**, 359–373 (1987).

76. Wang, Y. et al. Design principles for solid-state lithium superionic conductors. *Nat. Mater.* **14**, 1026–1031 (2015).

77. Torquato, S. Optimal design of heterogeneous materials. *Annu. Rev. Mater. Res.* **40**, 101–129 (2010).

78. Nan, C.-W. Physics of inhomogeneous inorganic materials. *Prog. Mater. Sci.* **37**, 1–116 (1993).

79. Jain, A., Bollinger, J. A. & Truskett, T. M. Inverse methods for material design. *AIChE J.* **60**, 2732–2740 (2014).

80. Nan, C. W. & Clarke, D. R. Effective properties of ferroelectric and/or ferromagnetic composites: a unified approach and its application. *J. Am. Ceram. Soc.* **80**, 1333–1340 (1997).

81. Srinivas, S. & Li, J. Y. The effective magnetoelectric coefficients of polycrystalline multiferroic composites. *Acta. Mater.* **53**, 4135–4142 (2005).

82. Liu, G., Nan, C. W. & Sun, J. Coupling interaction in nanostructured piezoelectric/magnetostrictive multiferroic complex films. *Acta. Mater.* **54**, 917–925 (2006).

83. Pertsev, N. A. Giant magnetoelectric effect via strain-induced spin reorientation transitions in ferromagnetic films. *Phys. Rev. B* **78**, 212102 (2008).

84. Li, J. Y. & Dunn, M. L. Micromechanics of magnetoelectroelastic composite materials: average fields and effective behavior. *J. Intell. Mater. Syst. Struct.* **9**, 404–416 (1998).

85. Srinivas, S., Li, J. Y., Zhou, Y. C. & Soh, A. K. The effective magnetoelectroelastic moduli of matrix-based multiferroic composites. *J. Appl. Phys.* **99**, 043905 (2006).

86. Nan, C. W., Bichurin, M. I., Dong, S. X., Viehland, D. & Srinivasan, G. Multiferroic magnetoelectric composites: historical perspective, status, and future directions. *J. Appl. Phys.* **103**, 031101 (2008).

Understanding and designing magnetoelectric heterostructures
J-M Hu et al.

19

87. Camacho-Montes, H., Rodriguez-Ramos, R., Bravo-Castillero, J., Guinovart-Diaz, R. & Sabina, F. J. Effective coefficients for two phase magneto-electroelastic fibrous composite with square symmetry cell in-plane mechanical displacement and out-of-plane electric and magnetic field case. *Integr. Ferroelectr.* **83**, 49–65 (2006).

88. Corcolle, R., Daniel, L. & Bouillault, F. Generic formalism for homogenization of coupled behavior: application to magnetoelectroelastic behavior. *Phys. Rev. B* **78**, 214110 (2008).

89. Ni, Y. & Khachaturyan, A. G. Phase field approach for strain-induced magneto-electric effect in multiferroic composites. *J. Appl. Phys.* **102**, 113506 (2007).

90. Zhang, J. X. et al. Phase-field model for epitaxial ferroelectric and magnetic nanocomposite thin films. *Appl. Phys. Lett.* **90**, 052909 (2007).

91. Chen, H. T., Hong, L. & Soh, A. K. Effects of film thickness and mismatch strains on magnetoelectric coupling in vertical heteroepitaxial nanocomposite thin films. *J. Appl. Phys.* **109**, 094102 (2011).

92. Yang, T. N., Hu, J.-M., Nan, C. W. & Chen, L. Q. Predicting effective magneto-electric response in magnetic-ferroelectric composites via phase-field modeling. *Appl. Phys. Lett.* **104**, 052904 (2014).

93. Ma, F. D. D., Jin, Y. M. M., Wang, Y. U., Kampe, S. L. & Dong, S. X. Effect of magnetic domain structure on longitudinal and transverse magnetoelectric response of particulate magnetostrictive-piezoelectric composites. *Appl. Phys. Lett.* **104**, 112903 (2014).

94. Van Lich, L. et al. Colossal magnetoelectric effect in 3-1 multiferroic nano-composites originating from ultrafine nanodomain structures. *Appl. Phys. Lett.* **107**, 232904 (2015).

95. Curtarolo, S., Morgan, D., Persson, K., Rodgers, J. & Ceder, G. Predicting crystal structures with data mining of quantum calculations. *Phys. Rev. Lett.* **91**, 135503 (2003).

96. Fischer, C. C., Tibbetts, K. J., Morgan, D. & Ceder, G. Predicting crystal structure by merging data mining with quantum mechanics. *Nat. Mater.* **5**, 641–646 (2006).

97. Bartók, A. P., Payne, M. C., Kondor, R. & Csányi, G. Gaussian approximation potentials: the accuracy of quantum mechanics, without the electrons. *Phys. Rev. Lett.* **104**, 136403 (2010).

98. Pilania, G., Wang, C., Jiang, X., Rajasekaran, S. & Ramprasad, R. Accelerating materials property predictions using machine learning. *Sci. Rep.* **3**, 2810 (2013).

99. Schütt, K. T. et al. How to represent crystal structures for machine learning: towards fast prediction of electronic properties. *Phys. Rev. B* **89**, 205118 (2014).

100. Seko, A., Maekawa, T., Tsuda, K. & Tanaka, I. Machine learning with systematic density-functional theory calculations: application to melting temperatures of single- and binary-component solids. *Phys. Rev. B* **89**, 054303 (2014).

101. Ward, L., Agrawal, A., Choudhary, A. & Wolverton, C. A general-purpose machine learning framework for predicting properties of inorganic materials. *npj Comput. Mater.* **2**, 16028 (2016).

102. Medasani, B. et al. Predicting defect behavior in B2 intermetallics by merging ab initio modeling and machine learning. *npj Comput. Mater.* **2**, 1 (2016).

103. Gaultois, M. W. et al. Perspective: web-based machine learning models for real-time screening of thermoelectric materials properties. *APL Mater.* **4**, 053213 (2016).

104. Duan, C.-G., Jaswal, S. S. & Tsymbal, E. Y. Predicted magnetoelectric effect in Fe/BaTiO$_3$ multilayers: ferroelectric control of magnetism. *Phys. Rev. Lett.* **97**, 047201 (2006).

105. Meyerheim, H. L. et al. Structural secrets of multiferroic interfaces. *Phys. Rev. Lett.* **106**, 087203 (2011).

106. Valencia, S. et al. Interface-induced room-temperature multiferroicity in BaTiO$_3$. *Nat. Mater.* **10**, 753–758 (2011).

107. Garcia, V. et al Ferroelectric control of spin polarization. *Science* **327**, 1106–1110 (2010).

108. Pantel, D., Goetze, S., Hesse, D. & Alexe, M. Reversible electrical switching of spin polarization in multiferroic tunnel junctions. *Nat. Mater.* **11**, 289–293 (2012).

109. Fechner, M., Zahn, P., Ostanin, S., Bibes, M. & Mertig, I. Switching magnetization by 180° with an electric field. *Phys. Rev. Lett.* **108**, 197206 (2012).

110. Vaz, C. A. F. et al. Origin of the magnetoelectric coupling effect in Pb(Zr$_{0.2}$Ti$_{0.8}$)O$_3$/La$_{0.8}$Sr$_{0.2}$MnO$_3$ multiferroic heterostructures. *Phys. Rev. Lett.* **104**, 127202 (2010).

111. Radaelli, G. et al. Electric control of magnetism at the Fe/BaTiO$_3$ interface. *Nat. Commun.* **5**, 3404 (2014).

112. Burton, J. D. & Tsymbal, E. Y. Prediction of electrically induced magnetic reconstruction at the manganite/ferroelectric interface. *Phys. Rev. B* **80**, 174406 (2009).

113. Burton, J. D. & Tsymbal, E. Y. Giant tunneling electroresistance effect driven by an electrically controlled spin valve at a complex oxide interface. *Phys. Rev. Lett.* **106**, 157203 (2011).

114. Yin, Y. W. et al. Enhanced tunnelling electroresistance effect due to a ferroelectrically induced phase transition at a magnetic complex oxide interface. *Nat. Mater.* **12**, 397–402 (2013).

115. Zheng, R. K. et al. Tuning the electrical properties of La$_{0.75}$Ca$_{0.25}$MnO$_3$ thin films by ferroelectric polarization, ferroelectric-field effect, and converse piezoelectric effect. *Phys. Rev. B* **74**, 094427 (2006).

116. Thiele, C., Dörr, K., Bilani, O., Rödel, J. & Schultz, L. Influence of strain on the magnetization and magnetoelectric effect in La$_{0.7}$A$_{0.3}$MnO$_3$/PMN-PT (001) (A=Sr, Ca). *Phys. Rev. B* **75**, 054408 (2007).

117. Pallecchi, I. et al. Field effect in manganite ultrathin films: magnetotransport and localization mechanisms. *Phys. Rev. B* **78**, 024411 (2008).

118. Stolichnov, I. et al. Non-volatile ferroelectric control of ferromagnetism in (Ga, Mn)As. *Nat. Mater.* **7**, 464–467 (2008).

119. Dhoot, A. S., Israel, C., Moya, X., Mathur, N. D. & Friend, R. H. Large electric field effect in electrolyte-gated manganites. *Phys. Rev. Lett.* **102**, 136402 (2009).

120. Chiba, D. et al. Electrical control of the ferromagnetic phase transition in cobalt at room temperature. *Nat. Mater.* **10**, 853–856 (2011).

121. Jiang, T. et al. Coaction and distinguishment of converse piezoelectric and field effects in La$_{0.7}$Ca$_{0.3}$MnO$_3$/SrTiO$_3$/0.68Pb(Mg$_{1/3}$Nb$_{2/3}$)O$_3$-0.32PbTiO$_3$ heterostructures. *Appl. Phys. Lett.* **103**, 053504 (2013).

122. Kim, H. K. D. et al. Magnetoelectric control of superparamagnetism. *Nano. Lett.* **13**, 884–888 (2013).

123. Wu, T. et al. Electroresistance and electronic phase separation in mixed-valent manganites. *Phys. Rev. Lett.* **86**, 5998–6001 (2001).

124. Liu, M. et al. Non-volatile ferroelastic switching of the Verwey transition and resistivity of epitaxial Fe$_3$O$_4$/PMN-PT (011). *Sci. Rep.* **3**, 1876 (2013).

125. Rondinelli, J. M. & Fennie, C. J. Octahedral rotation-induced ferroelectricity in cation ordered Perovskites. *Adv. Mater.* **24**, 1961–1968 (2012).

126. Xu, B. et al. Hybrid improper ferroelectricity in multiferroic superlattices: finite-temperature properties and electric-field-driven switching of polarization and magnetization. *Adv. Funct. Mater.* **25**, 3626–3633 (2015).

127. Puggioni, D., Giovannetti, G., Capone, M. & Rondinelli, J. M. Design of a Mott multiferroic from a nonmagnetic polar metal. *Phys. Rev. Lett.* **115**, 087202 (2015).

128. Mundy, J. A. et al. Atomically engineered ferroic layers yield a room-temperature magnetoelectric multiferroic. *Nature* **537**, 523–527 (2016).

129. Subramanian, M. A., Ramirez, A. P. & Marshall, W. J. Structural tuning of ferromagnetism in a 3D Cuprate Perovskite. *Phys. Rev. Lett.* **82**, 1558–1561 (1999).

130. Kim, T. H. et al. Polar metals by geometric design. *Nature* **533**, 68–72 (2016).

131. Hu, J.-M., Li, Z., Chen, L.-Q. & Nan, C.-W. High-density magnetoresistive random access memory operating at ultralow voltage at room temperature. *Nat. Commun.* **2**, 553 (2011).

132. Kanai, S. et al. Electric field-induced magnetization reversal in a perpendicular-anisotropy CoFeB-MgO magnetic tunnel junction. *Appl. Phys. Lett.* **101**, 122403 (2012).

133. Shiota, Y. et al. Induction of coherent magnetization switching in a few atomic layers of FeCo using voltage pulses. *Nat. Mater.* **11**, 39–43 (2012).

134. Bruno, P. Theory of interlayer magnetic coupling. *Phys. Rev. B* **52**, 411–439 (1995).

135. Zhuravlev, M. Y., Vedyayev, A. V. & Tsymbal, E. Y. Interlayer exchange coupling across a ferroelectric barrier. *J. Phys. Condens. Matter.* **22**, 352203 (2010).

136. Novosad, V. et al. Novel magnetostrictive memory device. *J. Appl. Phys.* **87**, 6400–6402 (2000).

137. Iwasaki, Y. Stress-driven magnetization reversal in magnetostrictive films with in-plane magnetocrystalline anisotropy. *J. Magn. Magn. Mater.* **240**, 395–397 (2002).

138. Wang, J. J. et al. Full 180° magnetization reversal with electric fields. *Sci. Rep.* **4**, 7507 (2014).

139. Peng, R.-C., Wang, J. J., Hu, J.-M., Chen, L.-Q. & Nan, C.-W. Electric-field-driven magnetization reversal in square-shaped nanomagnet-based multiferroic heterostructure. *Appl. Phys. Lett.* **106**, 142901 (2015).

140. Cowburn, R. P., Adeyeye, A. O. & Welland, M. E. Configurational anisotropy in nanomagnets. *Phys. Rev. Lett.* **81**, 5414–5417 (1998).

141. Yu, G. et al. Strain-induced modulation of perpendicular magnetic anisotropy in Ta/CoFeB/MgO structures investigated by ferromagnetic resonance. *Appl. Phys. Lett.* **106**, 072402 (2015).

142. Cui, J. et al. A method to control magnetism in individual strain-mediated magnetoelectric islands. *Appl. Phys. Lett.* **103**, 232905 (2013).

143. Peng, R.-C. et al. Fast 180° magnetization switching in a strain-mediated multiferroic heterostructure driven by a voltage. *Sci. Rep.* **6**, 27561 (2016).

144. Ghidini, M. et al. Non-volatile electrically-driven repeatable magnetization reversal with no applied magnetic field. *Nat. Commun.* **4**, 1453 (2013).

145. Hu, J.-M. et al. Purely electric-field-driven perpendicular magnetization reversal. *Nano. Lett.* **15**, 616–622 (2015).

146. Yi, M., Xu, B.-X. & Shen, Z. Magnetization switching in nanocylinders by a mechanical strain. *Extreme Mech. Lett.* **3**, 66–71 (2015).

147. Li, X. et al. Strain-mediated 180° perpendicular magnetization switching of a single domain multiferroic structure. *J. Appl. Phys.* **118**, 014101 (2015).

npj

Understanding and designing magnetoelectric heterostructures
J-M Hu et al.

20

148. Parkin, S. & Yang, S.-H. Memory on the racetrack. *Nat. Nanotechnol.* **10**, 195–198 (2015).

149. Chung, T.-K., Carman, G. P. & Mohanchandra, K. P. Reversible magnetic domain-wall motion under an electric field in a magnetoelectric thin film. *Appl. Phys. Lett.* **92**, 112509 (2008).

150. Sohn, H. et al. Electrically driven magnetic domain wall rotation in multiferroic heterostructures to manipulate suspended on-chip magnetic particles. *ACS Nano.* **9**, 4814–4826 (2015).

151. Franke, K. J. A. et al. Reversible electric-field-driven magnetic domain-wall motion. *Phys. Rev. X* **5**, 011010 (2015).

152. Haruka, K. et al. Switching local magnetization by electric-field-induced domain wall motion. *Appl. Phys. Express* **9**, 063004 (2016).

153. Dean, J., Bryan, M. T., Schrefl, T. & Allwood, D. A. Stress-based control of magnetic nanowire domain walls in artificial multiferroic systems. *J. Appl. Phys.* **109**, 023915 (2011).

154. Hu, J.-M. et al. Fast magnetic domain-wall motion in a ring-shaped nanowire driven by a voltage. *Nano. Lett.* **16**, 2341–2348 (2016).

155. Sahoo, S. et al. Ferroelectric control of magnetism in BaTiO$_3$/Fe heterostructures via interface strain coupling. *Phys. Rev. B* **76**, 092108 (2007).

156. Nan, T. et al Quantification of strain and charge co-mediated magnetoelectric coupling on ultra-thin Permalloy/PMN-PT interface. *Sci. Rep.* **4**, 3688 (2014).

157. Heidler, J. et al. Magnetoelectroelastic control of magnetism in an artificial multiferroic. *Phys. Rev. B* **94**, 014401 (2016).

158. Jedrecy, N. et al. Strong magnetoelectric coupling in multiferroic Co/BaTiO$_3$ thin films. *Phys. Rev. B* **88**, 121409 (2013).

159. Jia, C. L. et al. Mechanism of interfacial magnetoelectric coupling in composite multiferroics. *Phys. Rev. B* **90**, 054423 (2014).

160. Fan, Y. et al. Exchange bias of the interface spin system at the Fe/MgO interface. *Nat. Nanotechnol.* **8**, 438–444 (2013).

161. Lage, E. et al. Magnetic domain control and voltage response of exchange biased magnetoelectric composites. *Appl. Phys. Lett.* **104**, 132405 (2014).

162. Yadav, A. K. et al. Observation of polar vortices in oxide superlattices. *Nature* **530**, 198–201 (2016).

163. Wiesendanger, R. Nanoscale magnetic skyrmions in metallic films and multilayers: a new twist for spintronics. *Nat. Rev. Mater.* **1**, 16044 (2016).

164. James, G., Witten, D., Hastie, T.. & Tibshirani, R. *An Introduction to Statistical Learning: with Applications in R*, (Springer New York, 2013).

165. Larranaga, P. et al. Machine learning in bioinformatics. *Brief. Bioinform.* **7**, 86–112 (2006).

166. Libbrecht, M. W. & Noble, W. S. Machine learning applications in genetics and genomics. *Nat. Rev. Genet.* **16**, 321–332 (2015).

167. Banerji, M. et al. Galaxy Zoo: reproducing galaxy morphologies via machine learning. *Mon. Not. R. Astron. Soc.* **406**, 342–353 (2010).

168. Adam-Bourdarios, C. et al. The Higgs machine learning challenge. *J. Phys.: Conf. Ser.* **664**, 072015 (2015).

169. Jesse, S. et al. Band excitation in scanning probe microscopy: recognition and functional imaging. *Annu. Rev. Phys. Chem.* **65**, 519–536 (2014).

170. Belianinov, A. et al. Big data and deep data in scanning and electron microscopies: deriving functionality from multidimensional data sets. *Adv. Struct. Chem. Imag.* **1**, 6 (2015).

171. Kalinin, S. V. et al. Big, deep, and smart data in scanning probe microscopy. *ACS Nano.* **10**, 9068–9086 (2016).

172. Hattrick-Simpers, J. R., Gregoire, J. M. & Kusne, A. G. Perspective: composition–structure–property mapping in high-throughput experiments: turning data into knowledge. *APL Mater.* **4**, 053211 (2016).

173. Iwasaki, Y., Kusne, A. G. & Takeuchi, I. Comparison of dissimilarity measures for cluster analysis of X-ray diffraction data from combinatorial libraries. *npj Comput. Mater.* **3**, 4 (2017).

174. Raccuglia, P. et al. Machine-learning-assisted materials discovery using failed experiments. *Nature* **533**, 73–76 (2016).

175. Endo, M., Kanai, S., Ikeda, S., Matsukura, F. & Ohno, H. Electric-field effects on thickness dependent magnetic anisotropy of sputtered MgO/Co$_{40}$Fe$_{40}$B$_{20}$/Ta structures. *Appl. Phys. Lett.* **96**, 212503 (2010).

176. Mardana, A., Ducharme, S. & Adenwalla, S. Ferroelectric control of magnetic anisotropy. *Nano. Lett.* **11**, 3862–3867 (2011).

177. Wang, W.-G., Li, M., Hageman, S. & Chien, C. L. Electric-field-assisted switching in magnetic tunnel junctions. *Nat. Mater.* **11**, 64–68 (2012).

178. Grezes, C. et al. Ultra-low switching energy and scaling in electric-field-controlled nanoscale magnetic tunnel junctions with high resistance-area product. *Appl. Phys. Lett.* **108**, 012403 (2016).

179. Nozaki, T. et al Large voltage-induced changes in the perpendicular magnetic anisotropy of an MgO-based tunnel junction with an ultrathin Fe layer. *Phys. Rev. Appl.* **5**, 044006 (2016).

180. Eerenstein, W., Wiora, M., Prieto, J. L., Scott, J. F. & Mathur, N. D. Giant sharp and persistent converse magnetoelectric effects in multiferroic epitaxial heterostructures. *Nat. Mater.* **6**, 348–351 (2007).

181. Liu, M. et al. Giant electric field tuning of magnetic properties in multiferroic ferrite/ferroelectric heterostructures. *Adv. Funct. Mater.* **19**, 1826–1831 (2009).

182. Geprägs, S., Brandlmaier, A., Opel, M., Gross, R. & Goennenwein, S. T. B. Electric field controlled manipulation of the magnetization in Ni/BaTiO$_3$ hybrid structures. *Appl. Phys. Lett.* **96**, 142509 (2010).

183. Chen, Y., Fitchorov, T., Vittoria, C. & Harris, V. G. Electrically controlled magnetization switching in a multiferroic heterostructure. *Appl. Phys. Lett.* **97**, 052502 (2010).

184. Wang, J. et al. Large electric-field modulation of magnetic properties in Fe films on BiScO$_3$-PbTiO$_3$ ceramics. *J. Nanomater.* **2010**, 142750 (2010).

185. Brandlmaier, A., Geprägs, S., Woltersdorf, G., Gross, R. & Goennenwein, S. T. B. Nonvolatile, reversible electric-field controlled switching of remanent magnetization in multifunctional ferromagnetic/ferroelectric hybrids. *J. Appl. Phys.* **110**, 043913 (2011).

186. Lahtinen, T. H. E., Franke, K. J. A. & van Dijken, S. Electric-field control of magnetic domain wall motion and local magnetization reversal. *Sci. Rep.* **2**, 258 (2012).

187. Liu, M. et al Voltage tuning of ferromagnetic resonance with bistable magnetization switching in energy-efficient magnetoelectric composites. *Adv. Mater.* **25**, 1435–1439 (2013).

188. Shirahata, Y. et al. Electric-field switching of perpendicularly magnetized multilayers. *NPG Asia Mater.* **7**, e198 (2015).

189. Tkach, A. et al. Electric field modification of magnetotransport in Ni thin films on (011) PMN-PT piezosubstrates. *Appl. Phys. Lett.* **106**, 062404 (2015).

190. Chen, A. et al. Angular dependence of exchange bias and magnetization reversal controlled by electric-field-induced competing anisotropies. *Adv. Mater.* **28**, 363–369 (2016).

191. Liu, Y. et al. Electric-field control of magnetism in Co$_{40}$Fe$_{40}$B$_{20}$/(1-x)Pb(Mg$_{1/3}$Nb$_{2/3}$)O$_3$-xPbTiO$_3$ multiferroic heterostructures with different ferroelectric phases. *ACS Appl. Mater. Interfaces* **8**, 3784–3791 (2016).

192. Cherifi, R. O. et al. Electric-field control of magnetic order above room temperature. *Nat. Mater.* **13**, 345–351 (2014).

193. Van Den Boomgaard, J., Van Run, A. M. J. G. & Suchtelen, J. V. Magnetoelectricity in piezoelectric-magnetostrictive composites. *Ferroelectrics* **10**, 295–298 (1976).

194. van den Boomgaard, J. & Born, R. A. J. A sintered magnetoelectric composite material BaTiO$_3$-Ni(Co, Mn)Fe$_2$O$_4$. *J. Mater. Sci.* **13**, 1538–1548 (1978).

195. Srinivasan, G., DeVreugd, C. P., Flattery, C. S., Laletsin, V. M. & Paddubnaya, N. Magnetoelectric interactions in hot-pressed nickel zinc ferrite and lead zirconante titanate composites. *Appl. Phys. Lett.* **85**, 2550–2552 (2004).

196. Ryu, J., Carazo, A. V., Uchino, K. & Kim, H.-E. Piezoelectric and magnetoelectric properties of Lead Zirconate Titanate/Ni-Ferrite particulate composites. *J. Electroceram.* **7**, 17–24 (2001).

197. Arif, D. S. & Mathe, V. L. Effect of the piezomagnetic NiFe$_2$O$_4$ phase on the piezoelectric Pb(Mg$_{1/3}$Nb$_{2/3}$)$_{0.67}$Ti$_{0.33}$O$_3$ phase in magnetoelectric composites. *Smart Mater. Struct.* **18**, 065014 (2009).

198. Zhai, J., Cai, N., Shi, Z., Lin, Y. & Nan, C.-W. Magnetic-dielectric properties of NiFe$_2$O$_4$/PZT particulate composites. *J. Phys. D: Appl. Phys.* **37**, 823–827 (2004).

199. Islam, R. A. & Priya, S. Synthesis of high magnetoelectric coefficient composites using annealing and aging route. *Int. J. Appl. Ceram. Tec.* **3**, 353–363 (2006).

200. Zhang, J. X. et al. The effect of magnetic nanoparticles on the morphology, ferroelectric, and magnetoelectric behaviors of CFO/P(VDF-TrFE) 0–3 nanocomposites. *J. Appl. Phys.* **105**, 054102 (2009).

201. Wan, J. G. et al. Magnetoelectric CoFe$_2$O$_4$–Pb(Zr,Ti)O$_3$ composite thin films derived by a sol-gel process. *Appl. Phys. Lett.* **86**, 122501 (2005).

202. Ryu, H. et al. Magnetoelectric effects of nanoparticulate Pb(Zr$_{0.52}$Ti$_{0.48}$)O$_3$–NiFe$_2$O$_4$ composite films. *Appl. Phys. Lett.* **89**, 102907 (2006).

203. Chee-Sung, P. et al. Giant magnetoelectric coefficient in 3–2 nanocomposite thick films. *Jpn. J. Appl. Phys.* **48**, 080204 (2009).

204. Li, Y. et al. Magnetoelectric quasi-(0-3) nanocomposite heterostructures. *Nat. Commun.* **6**, 6680 (2015).

205. Palneedi, H. et al. Unleashing the full potential of magnetoelectric coupling in film heterostructures. *Adv. Mater.* **29**, 1605688 (2017).

206. Ryu, J., Priya, S., Uchino, K. & Kim, H.-E. Magnetoelectric effect in composites of magnetostrictive and piezoelectric materials. *J. Electroceram.* **8**, 107–119 (2002).

207. Zhai, J., Dong, S., Xing, Z., Li, J. & Viehland, D. Giant magnetoelectric effect in Metglas/polyvinylidene-fluoride laminates. *Appl. Phys. Lett.* **89**, 083507 (2006).

208. Israel, C., Mathur, N. D. & Scott, J. F. A one-cent room-temperature magnetoelectric sensor. *Nat. Mater.* **7**, 93–94 (2008).

209. Laletin, U. et al. Hysteresis and remanence in magnetoelectric effects in functionally graded magnetostrictive-piezoelectric layered composites. *Phys. Rev. B* **85**, 104404 (2012).

Understanding and designing magnetoelectric heterostructures
J-M Hu et al.

npj

21

210. Zhou, Y., Yang, S. C., Apo, D. J., Maurya, D. & Priya, S. Tunable self-biased magnetoelectric response in homogenous laminates. *Appl. Phys. Lett.* **101**, 232905 (2012).

211. Yan, Y., Zhou, Y. & Priya, S. Giant self-biased magnetoelectric coupling in co-fired textured layered composites. *Appl. Phys. Lett.* **102**, 052907 (2013).

212. Lu, M.-C. et al. Enhancing the magnetoelectric response of Terfenol-D/poly-vinylidene fluoride/Terfenol-D laminates by exploiting the shear mode effect. *Appl. Phys. Lett.* **106**, 112905 (2015).

213. Fang, Z. et al. Enhancing the magnetoelectric response of Metglas/poly-vinylidene fluoride laminates by exploiting the flux concentration effect. *Appl. Phys. Lett.* **95**, 112903 (2009).

214. Dong, S., Zhai, J., Li, J. & Viehland, D. Near-ideal magnetoelectricity in high-permeability magnetostrictive/piezofiber laminates with a (2-1) connectivity. *Appl. Phys. Lett.* **89**, 252904 (2006).

215. Dong, S., Zhai, J., Xing, Z., Li, J. & Viehland, D. Giant magnetoelectric effect (under a dc magnetic bias of 2Oe) in laminate composites of FeBSiC alloy ribbons and $Pb(Zn_{1/3}Nb_{2/3})O_3$–7%$PbTiO_3$ fibers. *Appl. Phys. Lett.* **91**, 022915 (2007).

216. Wang, Y. J. et al. An extremely low equivalent magnetic noise magnetoelectric sensor. *Adv. Mater.* **23**, 4111–4114 (2011).

217. Li, M. H., Wang, Z. G., Wang, Y. J., Li, J. F. & Viehland, D. Giant magnetoelectric effect in self-biased laminates under zero magnetic field. *Appl. Phys. Lett.* **102**, 082404 (2013).

218. Deng, C., Zhang, Y., Ma, J., Lin, Y. & Nan, C.-W. Magnetic-electric properties of epitaxial multiferroic $NiFe_2O_4$–$BaTiO_3$ heterostructure. *J. Appl. Phys.* **102**, 074114 (2007).

219. Zhang, Y., Deng, C., Ma, J., Lin, Y. & Nan, C.-W. Enhancement in magnetoelectric response in $CoFe_2O_4$-$BaTiO_3$ heterostructure. *Appl. Phys. Lett.* **92**, 062911 (2008).

220. He, H. C., Ma, J., Lin, Y. H. & Nan, C. W. Enhanced magnetoelectric properties in $Pb(Zr,Ti)O_3$-$CoFe_2O_4$ layered thin films with $LaNiO_3$ as a buffer layer. *J. Phys. D: Appl. Phys.* **42**, 095008 (2009).

221. Ryu, S., Park, J. H. & Jang, H. M. Magnetoelectric coupling of [00l]-oriented $Pb(Zr_{0.4}Ti_{0.6})O_3$–$Ni_{0.8}Zn_{0.2}Fe_2O_4$ multilayered thin films. *Appl. Phys. Lett.* **91**, 142910 (2007).

222. Ma, Y. G., Cheng, W. N., Ning, M. & Ong, C. K. Magnetoelectric effect in epitaxial $Pb(Zr_{0.52}Ti_{0.48})O_3$/$La_{0.7}Sr_{0.3}MnO_3$ composite thin film. *Appl. Phys. Lett.* **90**, 152911 (2007).

223. Greve, H., Woltermann, E., Quenzer, H.-J., Wagner, B. & Quandt, E. Giant magnetoelectric coefficients in $(Fe_{90}Co_{10})_{78}Si_{12}B_{10}$-AlN thin film composites. *Appl. Phys. Lett.* **96**, 182501 (2010).

224. Wang, J., Zhang, Y., Ma, J., Lin, Y. & Nan, C. W. Magnetoelectric behavior of $BaTiO_3$ films directly grown on $CoFe_2O_4$ ceramics. *J. Appl. Phys.* **104**, 014101 (2008).

225. Wang, J., Li, Z., Shen, Y., Lin, Y. & Nan, C. W. Enhanced magnetoelectric coupling in $Pb(Zr_{0.52}Ti_{0.48})O_3$ film-on-$CoFe_2O_4$ bulk ceramic composite with $LaNiO_3$ bottom electrode. *J. Mater. Sci.* **48**, 1021–1026 (2013).

226. Liang, W. et al. Role of the interface on the magnetoelectric properties of $BaTiO_3$ thin films deposited on polycrystalline Ni foils. *J. Mater. Chem. C* **2**, 708–714 (2014).

227. Feng, M. et al. Optimizing direct magnetoelectric coupling in $Pb(Zr,Ti)O_3$/Ni multiferroic film heterostructures. *Appl. Phys. Lett.* **106**, 072901 (2015).

228. Lorenz, M. et al. Epitaxial coherence at interfaces as origin of high magneto-electric coupling in multiferroic $BaTiO_3$–$BiFeO_3$ superlattices. *Adv. Mater. Interfaces* **3**, 1500822 (2016).

229. Chu, Z. et al. Enhanced resonance magnetoelectric coupling in (1-1) connectivity composites. *Adv. Mater.* 1606022 (2017). doi:10.1002/adma.201606022.

230. Ma, J., Shi, Z. & Nan, C. W. Magnetoelectric properties of composites of single $Pb(Zr,Ti)O_3$ rods and Terfenol-D/Epoxy with a single-period of 1-3-type structure. *Adv. Mater.* **19**, 2571–2573 (2007).

231. Xie, S., Ma, F., Liu, Y. & Li, J. Multiferroic $CoFe_2O_4$-$Pb(Zr_{0.52}Ti_{0.48})O_3$ core-shell nanofibers and their magnetoelectric coupling. *Nanoscale* **3**, 3152–3158 (2011).

232. Ma, J., Hu, J., Li, Z. & Nan, C.-W. Recent progress in multiferroic magnetoelectric composites: from bulk to thin films. *Adv. Mater.* **23**, 1062–1087 (2011).

233. Nakaya, Y. & Mori, H. Magnetocardiography. *Clin. Phys. Physiol. Meas.* **13**, 191–229 (1992).

234. Wikswo, J. P. Jr. SQUID magnetometers for biomagnetism and nondestructive testing: important questions and initial answers. *IEEE Trans. Appl. Supercond.* **5**, 74–120 (1995).

235. LeCun, Y., Bengio, Y. & Hinton, G. Deep learning. *Nature* **521**, 436–444 (2015).

236. Valpola, H. *Bayesian ensemble learning for nonlinear factor analysis*, (Doctoral dissertation, Helsinki University of Technology, 2000).

237. Groeber, M. A. & Jackson, M. A. DREAM.3D: a digital representation environment for the analysis of microstructure in 3D. *Integrating Mater.* **3**, 1–17 (2014).

238. Krill, C. E. & Chen, L. Q. Computer simulation of 3-D grain growth using a phase-field model. *Acta. Mater.* **50**, 3057–3073 (2002).

239. Kalnaus, S. et al. Effective conductivity of particulate polymer composite electrolytes using random resistor network method. *Solid State Ion.* **199–200**, 44–53 (2011).

240. Chen, L. Q. Phase-field models for microstructure evolution. *Annu. Rev. Mater. Res.* **32**, 113–140 (2002).

241. Liu, R. et al. A predictive machine learning approach for microstructure optimization and materials design. *Sci. Rep.* **5**, 11551 (2015).

242. Kirklin, S. et al. The open quantum materials database (OQMD): assessing the accuracy of DFT formation energies. *npj Comput. Mater.* **1**, 15010 (2015).

243. Liu, W. & Ren, X. Large piezoelectric effect in Pb-free ceramics. *Phys. Rev. Lett.* **103**, 257602 (2009).

244. Yang, S. et al. Large magnetostriction from morphotropic phase boundary in ferromagnets. *Phys. Rev. Lett.* **104**, 197201 (2010).

245. McDowell, D. L. & LeSar, R. A. The need for microstructure informatics in process–structure–property relations. *MRS Bull.* **41**, 587–593 (2016).